ABSTRACT

CLARK III, BEVERLY A. Split-tip Scanning Capacitance Microscopy (SSCM): Special Techniques in Surface Characterization and Measurements. (Under the direction of Professor Hans Hallen).

This work invents and develops a new technique for electrical, electro-optical, and topographical characterization at the nanoscale. Split-tip scanning capacitance microscopy (SSCM) offers advantages over other scanning probe methods. The dependence of the measurements on sample characteristics is reduced, and analysis is simplified by having both electrodes secured to the probe. This feature allows non-conducting, as well as conducting surfaces to be imaged without loss of optical or capacitance resolution. SSCM allows surface measurements without destroying the sample of interest and does not require special surface preparation. To develop this new technique, the project focused on the following:

- shear-force feedback as an accurate tip-sample distance controller
- imaging techniques for irregular sample surfaces
- development of computational model for simulating split-tip measurements
- split-tip integration into a conventional near-field scanning optical microscope
- contrast modeling for surface structures
- tip-sample approach capacitance measurements as a stringent test of SSCM.

We show that a non-linear tip sample interaction dominates the shear force feedback signal evidenced by a change in the resonance frequency as the tip approaches the sample. Shear force feedback relies on a decrease in the signal amplitude at the operating frequency. We present data and a numerical model describing the time response and how this nonlinear interaction can be used to speed up the response.

We demonstrate the imaging of irregular surfaces such as paint samples and show the distribution of pigment quantified by the peak in the histogram of optical signal versus separation at the nano- to micron scale illuminates the length-scale of failure in paint samples. We compare a high quality paint sample with one that fails a standard quality control test based upon visual inspection. Features such as pigment clumping and pigment density fluctuations are simultaneously analyzed. Individual pigment particles are observed near the polymer surface of both samples.

We develop a split-tip model that yields the capacitance across the split-tip and also gives related insights into the origins of the features and behaviors via related calculated values such as charge and energy density. We elucidate these properties using computational finite element methods for several simple examples. The model yields insights into resolution and field enhancement effects near the probe edges.

We describe the fabrication of the novel split-tip optical nanoprobe that is used in the SSCM setup. The split-tip nanoprobe can be used to both orient molecules with a strong, localized electric field and deposit them, and to measure capacitance, energy density, and charge. The process for mounting this probe for integration in SSCM is also described; this mounting process allows reliable contact to be made to each probe electrode while meeting the stringent requirements for shear-force feedback with the probe. Data is collected from the split-tip with the use of a capacitance bridge circuit integrated into the scanning probe setup.

Lastly experimental measurements with the SSCM tie the above results together. Split-tip capacitance measurements with respect to tip-sample distance provide a critical test of the models and instrument capabilities. Approach capacitance measurements show the

ability to distinguish between different sample surfaces by measuring the capacitance between the probe electrodes and how it varies with respect to distance from the sample surface. We present approach capacitance measurements made on a sample comprised of aluminum structures deposited on a silica substrate grating. The experimental data is compared with the finite element model to gain more insights on the localized edge effects caused by field enhancements just under the split-tip probe.

Split-tip Scanning Capacitance Microscopy (SSCM): Special Techniques in Surface Characterization and Measurements

by
Beverly Andrew Clark, III

A dissertation submitted to the Graduate Faculty of
North Carolina State University
in partial fulfillment of the
requirements for the Degree of
Doctor of Philosophy

Physics

Raleigh, North Carolina

2009

APPROVED BY:

Dr. H.D. Hallen Chair of Advisory Committee	Dr. C. Roland
Dr. M. Paesler	Dr. W. Alexander

DEDICATION

I dedicate this dissertation to my mother, Althera Clark.

A woman who taught me education was important through example.

A woman who taught me to be dedicated and steadfast even in the bleakest hour.

A woman of valor and character.

A woman with extreme devotion to education.

A woman who sacrificed so that I would succeed.

A woman I love with all my heart.

In loving memory of:

Booker & Gladys Callands,

Beatrice Clark,

and

Kathy Glass

BIOGRAPHY

In 1976, Beverly was born in rural Virginia to Althera and Beverly Clark, Jr. and grew up in a modest home located in Java. At an early age, Beverly found an interest in science and music, and both have been constants throughout his life. He was educated in Pittsylvania County Public Schools graduating from Chatham High School in 1994. Upon completion of high school, Beverly attended Emory & Henry College (E&H) and majored in Physics. During his time at E&H, Beverly was involved in numerous on and off campus activities. Along with studying physics, Beverly was a four-year letterman on the E&H football team, a resident advisor, and bassist for the college gospel choir (Spiritual Harmony), co-founded by Beverly and numerous other students. After graduating in 1999 with a Bachelor of Science, Beverly taught English as a second language in Lins, Brasil before entering the graduate program at North Carolina State University (NCSU).

At NCSU, Beverly immediately started working for Hans Hallen in the Near-Field Optics Lab quickly learning the basics of scanning probe microscopy. During his graduate career, Beverly was a General Electric Fellow as well as a Graduate Assistant in Areas of National Need (GAANN) Fellow. In 2003, Beverly received a Masters of Science from NCSU and continued with his graduate studies. From 2003-2004 he also served as president of the NCSU Association for the Concerns of African American Graduate Students (ACAAGS). While completing his graduate work, Beverly has played bass guitar and

saxophone for numerous local and national recording artists such as Chrisette Michele, Kevin Hill (K-Hill), Tyrand, and many others.

On June 10, 2009 Beverly successfully defended his Doctorate of Philosophy in Physics, completing his graduate studies. Science and music have remained constants in Beverly's life, and he continues to do both with excitement and zeal.

ACKNOWLEDGEMENTS

I would like to acknowledge some of the many people who have helped and supported me during my graduate studies.

I would like to thank my research advisor Dr. Hans Hallen. Over the years, you have helped me more than you will ever know. Since 1998 (summer REU Program), you have been instrumental in my development as a scientist, and I will always be grateful for your assistance and guidance.

To my advisory committee (Dr. H. Hallen, Dr. C. Roland, Dr. M. Paesler, and Dr. W. Alexander), I would like to thank you for your insight on all aspects of my academic work and research. I extend a special thanks to Dr. Paesler for his continuous guidance and encouragement throughout my graduate studies.

Special thanks to the National Science Foundation for support through grants DMR-9975543 and DMII-0210058, the Research Corporation through grant CC5342, and the U.S. Department of Education Graduate Assistance in Areas of National Need (GAANN) Fellowship Program (P200A000854). Thanks Gamil Guirgis for providing the paint samples imaged in Chapter 3.

Thanks to the members of the NCSU Near-field Optics Group especially Jeremy Peters, Trey Walker, and Ryan Neely for the enjoyable, thought-provoking conversations and friendship.

To Dr. Mike Taylor and Dr. Christopher Chadwick: it has been an eventful 10 years with numerous ups and downs. It has been filled with lab relocations, water leaks, and flash floods, but we all made it through thanks to the support we have shown one another. We have definitely been banded together in brotherhood through this experience, and I will always cherish the friendships we have formed.

Lastly, I would like to thank Angela Combs Richardson for being a source of support and encouragement during the completion of my graduate work. I truly appreciate all the kind words and every act of support you have shown me. I love you and thank God for your loving spirit and presence in my life. You made a rough road seem smooth.

TABLE OF CONTENTS

LIST OF FIGURES ... ix
1. Introduction ... 1
1.1 Bibliography ... 5
2. Shear-force Feedback ... 7
2.1 Nonlinear Tip-Sample Interaction ... 7
2.2 Data Analysis ... 16
2.3 Bibliography ... 17
3. Imaging Techniques of Irregular Surfaces ... 19
3.1 Introductory NSOM ... 19
3.2 Imaging Methods ... 20
3.3 Imaging Results ... 21
3.4 Single Pigment Particle Imaging ... 25
3.5 Data Analysis ... 27
3.6 Bibliography ... 29
4. Novel Split-Tip Proximal Probe for SSCM and Fabrication of Nanometer-Textured, In-Plane Oriented Polymer Films ... 30
4.1 Introduction ... 30
4.2 Probe Fabrication Methods ... 33
4.2.1 Probe Design Criteria ... 33
4.2.2 Probe Fabrication ... 34
4.2.3 Probe Mounting ... 37
4.2.4 Probe Usage ... 39
4.3 Results & Discussion ... 40
4.4 Data Analysis ... 46
4.5 Bibliography ... 48
5. Split-Tip Scanning Capacitance Microscopy (SSCM): A Finite Element Model ... 50
5.1 Introductory Modeling ... 50
5.2 Model Methods ... 52
5.2.1 Lateral Capacitance Scans ... 54
5.2.2 Approach Capacitance Scans ... 56
5.2.3 Dopant Density Scans ... 58
5.3 Model Results and Discussion ... 59
5.4 Data Analysis ... 63
5.5 Bibliography ... 65
6. Split-Tip Scanning Capacitance Microscopy (SSCM) ... 66
6.1 Introductory Split-Tip Scanning Capacitance ... 66
6.2 SSCM Split-tip Holder ... 67
6.3 Capacitance Sensor ... 70

6.4 Sample Grating 70
6.5 Measurement Sequence 71
6.6 SSCM Experimental Results 72
6.7 SSCM Data Analysis 82
6.8 Bibliography 84
7. Dissertation Conclusions 85

LIST OF FIGURES

Figure 2. 1: (a) Typical resonance curves obtained with the tuning fork method of oscillation amplitude measurement at various tip-sample separations (solid lines). (b) Resonance curves with different degrees of tapping obtained by a numerical solution of the nonlinear differential equation. 8
Figure 2. 2: (a) The numerical calculation of the time response for the feedback signal to drop to 1/e for a variety of driving frequencies for two situations: turning the tapping off and turning the tapping on. This time response is overlaid with the resonance curve for reference. (b) The experimental time response for the probe to find the surface with optimized gain given an 8msec-ramped trapezoidal step of height 30 nm. 11
Figure 2. 3: The feedback response to an impulse of 40 nm on the z-piezo for a variety of driving frequencies on either side of the resonant frequency with constant gain. The black lines are the outward motion. The grey lines are the inward motion. The resonance curve is overlaid for reference. 13
Figure 2. 4: Experimental resonance curves showing the undamped resonance, a resonance at 35% of the free resonance and a clamped resonance curve. The peak of the clamped resonance is only 2% of the undamped resonance peak, and the frequency shift is ~400Hz. 14
Figure 3. 1: This is a topographic scan of the reference sample (1905nm x 1905nm). The axes are in nanometers. The overall z distance range is 1138nm. The middle region of the image represents one plateau at a vertical position near 228nm. The upper middle portion of the image is 187nm above the middle plateau, and the bottom right where polymer ridging is observed is 663nm below the middle plateau. 23
Figure 3. 2: This is an optical scan of the reference sample (1905nm x 1905nm). The optical range was measured in arbitrary units. The horizontal axis is in nanometers. There is an overall optical range of 0.051a.u. In the upper left and lower right portions of the image, polymer ridging is observed. This is consistent with Figure 3.1, which was taken over the same scan range. 24
Figure 3. 3: This is an optical scan of the low quality sample (3175nm x 3175nm). The horizontal axis is in nanometers. There is an overall optical range of 0.27a.u. The scan shows pigment particle clumping in a non-uniform manner. Although the arrangement is non-uniform, it is still possible to identify pigment particles (see Figure 3.5). 25
Figure 3. 4: (a) is a histogram of the optical variation and (b) a histogram of the topographical variation. In analyzing the percent variation, it is possible to distinguish between the reference and low quality sample. 26
Figure 3. 5: This is the optical forward/backward line-cut data from the lower portion of Figure 3.3. The forward data have been shifted upward for clarity. The horizontal axis is distance (nm), and the vertical axis is in arbitrary units. The forward data (top graph) is shifted to the right of the back data (bottom graph) due to hysteresis. The arrows indicate

corresponding data points in the forward and backward data that reflect the same pigment particles. 27
Figure 4. 1: The split-tip probe has electrodes on the left and right sides, and the aperture located at the bottom. 32
Figure 4. 2: Figure shows a schematic of the split-tip near the sample as molecules are deposited. 33
Figure 4. 3: SEM image of a larger-aperture tapered fiber fabricated by the heat-and-pull method. Note the flat cleaved end that is formed when this fabrication scheme is used, as opposed to the sharp point of etched fibers. 35
Figure 4. 4: The end of a split-tip fabrication with the optimal fabrication procedures. 37
Figure 4. 5: A photograph of the tip holder; a piece of glass shaped to hold the tip on a tuning fork (upper right portion), the Teflon holder on the upper left keeps the gold wires positioned for contact with the fiber. The fiber can be seen passing through the groove in the Teflon where it contacts the wires, and on to the tuning fork (partially hidden). 38
Figure 4. 6: (a) shows split-tip probe fabricated with certain imperfections, such as voids in the coating. (b) shows cracking and peeling which presents a significant problem. (c) shows tensile stress. 41
Figure 4. 7: Figure shows a detailed view of the separation between the split-tip electrodes. The split is not completely void, containing small grains of material. 45
Figure 5. 1: Image of the split-tip probe positioned over a nanorod and substrate. The split is perpendicular to the rod and substrate. 54
Figure 5. 2: Split tip rotated about y axis by 90 degrees. 55
Figure 5. 3: Split-tip probe is located 10nm above the substrate surface. Aluminum and silica substrates were scanned varying the vertical distance in y. 57
Figure 5. 4: Boundary conditions slightly modified for dopant density measurements. Substrate has conductivity varied and capacitance measurements made. 59
Figure 5. 5: This is a plot of the lateral capacitance between the split-tip probe electrodes with the split parallel to the nanorod and substrate. 60
Figure 5. 6: This is a plot of the lateral capacitance between the split-tip probe electrodes with the split perpendicular to the nanorod and substrate. 61
Figure 5. 7: Plot of the capacitance between the electrodes. The horizontal axis shows vertical absolute values labeled d. 62
Figure 5. 8: Graph shows the capacitances calculated for n-type materials with different conductivities. 63
Figure 6. 1: Image of Standard NSOM setup with PMT (top left) used for optical data collection. The probe and tuning fork are mounted to the glass tip holder, with the sample mounted to the piezo electric tube for fine adjustment (top center). Course adjustment is achieved with a stepper motor (right middle). 68
Figure 6. 2: Split-tip can be adjusted to make attachment to the tuning fork tip holder used in SSCM. Holder has adjustable V-groove clamp to secure the split-tip. 69

Figure 6. 3: This is a plot of the experimental data taken from the aluminum grating structure. There were 2000 capacitance points read in over a 750nm z-range. 73
Figure 6. 4: Plot of approach capacitance versus z from the aluminum grating structure. The 0-550nm range spans over regions (a) and (b) from Figure 6.3. 75
Figure 6. 5: This is a plot of the experimental data taken from the aluminum grating structure (shown in Figure 6.3) with the sample surface correctly shifted to z = 173nm and the drift from the capacitance bridge circuit removed. 76
Figure 6. 6: Plot shows various aluminum capacitance profiles taken from Figure 6.5. Plot compares capacitance profiles for two different data sets taken near the sample surface. The vertical axis shows Capacitance (pF) and z (nm), shown on the horizontal axis, give the distance near the sample surface. 77
Figure 6. 7: This is a plot of the experimental data taken from the silica grating structure. There were 2000 capacitance points read in over a 750nm z range. 78
Figure 6. 8: Plot of the silica approach capacitance versus z values taken from region (b) of Figure 6.7. 79
Figure 6. 9: Plot shows various silica capacitance data sets taken near the surface. The capacitance is plotted as a function of the z values to more accurately compare the capacitance profiles near the sample surface. 80
Figure 6. 10: Plots compare various experimental capacitance profiles from aluminum and silica sample scans to the Femlab model values. The green line indicates the range of data comparable to the Femlab model, which is the first 25nm of capacitance values. 81
Figure 6. 11: Femlab aluminum model data plotted with the inbound/outbound aluminum experimental data. 1/z curve (solid line) is fit to one set of the aluminum experimental data, which appropriately describes the behavior of the aluminum experimental data well away from the sample surface. 82

Chapter 1

1. Introduction

This work invents and develops a new technique for electrical, electro-optical, and topographical characterization at the nanoscale. Split-tip scanning capacitance microscopy (SSCM) offers some advantages over other scanning probe methods. The dependence of the measurements on sample characteristics is reduced, and the analysis is simplified by having both electrodes secured to the probe. SSCM differs from the related, single tip AFM-based versions by having both electrodes secured to the probe [1,2,3]. This reduces the dependence of the measurements on sample characteristics and simplifies the analysis [4]. SSCM allows the imaging of simultaneous topographic, optical, and electronic structures [5,6]. This feature allows non-conducting, as well as conducting surfaces to be imaged without loss of optical resolution[7]. The newly developed split-tip is a dual electrode probe that allows

measurements in a non-contact manner. Unlike conventional scanning capacitance methods, SSCM allows measurements without destroying the sample of interest. To develop this new technique, the project focused on the following concepts:

- shear-force feedback as an accurate tip-sample distance controller [8,9,10]
- imaging techniques for irregular sample surfaces [11]
- computational models or simulating split-tip measurements
- split-tip integration into a conventional near-field scanning optical microscope
- contrast modeling for simple surface structures
- tip-sample approach capacitance measurements as a stringent test of SSCM.

The project first focused on improving the shear-force feedback process for high-resolution imaging. To improve the shear force feedback of the experimental setup, we exploit the non-linear tip sample interaction which relies on a decrease in the amplitude of the signal at the resonance frequency. This decrease occurs due to an increase in the quality factor (Q) and a high frequency shift in the resonance. The resonance shift is also a result of the nonlinear tip-sample interaction. The change in Q is slow, while the frequency shift is fast [8, 9, 10, 12]. This process has proven effective in the SSCM experimental setup and has improved data collection.

Next, the project shifted to imaging techniques and statistical analysis. Paint samples, with irregular surfaces, were resolved revealing mesoscopic distributions of pigment and several single pigment particles [11]. Statistical analysis of the mesoscopic data showed that

the best distribution is peaked on a mesoscopic scale. Single pigment particle imaging provided insight on the optical resolution, since the pigment particles were on the order of the imaging resolution. This project provided needed insight into imaging rough, irregular surfaces.

After improvement on feedback and imaging techniques, the focus shifted to developing a split-tip holder, fitting the split-tip probe into the V-groove holder that provided stability and reproducibility. Simultaneously we developed a model to provide insights on capacitance values found from finite element measurements, and collecting capacitance measurements from the SSCM experimental setup.

Novel fabrication schemes are required to deposit nanoscale materials that contain molecules oriented in the plane of the surface [13]. We present the fabrication of a novel split-tip optical nanoprobe that can be used to both orient the molecules with a strong, localized electric field and deposit them with nanoscale resolution. Ultraviolet light injected through the probe into the region of aligned molecules completes the deposition. The production of the split-tip probe is significantly different than that of the related near-field scanning optical microscope (NSOM) probe [14, 15], due to film stress issues. Mounting of the probe to insure reliable electrical contacts is also described.

Lastly, the capacitance properties are elucidated using computational (finite element) methods [16, 17]. The computational model also yields insight into resolution and field enhancement effects near the probe edges. From a simple capacitor model, knowledge is

applied in developing a more complicated, but still symmetrical model. The results indicate that local measurements of doping levels in semiconductors is possible. Values obtained from the finite element model are compared to SSCM experimental values. The more advanced model of the split-tip probe yields results of capacitance and other related values such as energy density and charge. Approach capacitance measurements from the SSCM experimental setup are presented and discussed. From the on (aluminum) and off (silica) grating capacitance measurements, properties like charge, energy density, and capacitance are distinguished.

This comprises the body of work for this dissertation.

1.1 Bibliography

1. Stefan Lanyi and Miloslav Hruskovic, J. Phys. D Appl. Phys. **36,** 598 (2003).

2. H.D. Hallen, A.H. La Rosa and C.L. Jahncke, Phys. Stat. Sol. (a) **152,** 257 (1995).

3. A.H. La Rosa, B.I. Yakobson, and H.D. Hallen, Mater. Res. Soc. Symp. Proc. **406,** 189 (1995).

4. H.E. Ruda and A. Shik, Phys. Rev. Lett. B **67,** 235309 (2003).

5. K. Karrai and R. Grober, Proc. SPIE **2535**, 69 (1995).

6. R. Brunner, A. Bietsch, O. Hollricher, and O. Marti, Rev. Sci. Instrum. **68**, 1769 (1997).

7. E. Betzig, P. Finn, and J.S. Weiner, Appl. Phys. Lett. **60,** 2484 (1992).

8. X.S. Xie and R.C. Dunn, Science **265**, 361 (1994).

9. E.J. Ayers, H.D. Hallen, and C.L. Jahncke, Phys. Rev. Lett. **85**, 4180 (2000).

10. S.H. Huerth, M.P. Taylor, H.D. Hallen, and B.H. Moeckley, Appl. Phys. Lett. **77**, 2127 (2000).

11. B. Clark III, G. Gurguis, H.D. Hallen, J. Vac. Sci. Technol. B **25,** 54 (2007).

12. C.L. Jahncke, S.H. Heurth, B. Clark III, and H.D. Hallen, Appl. Phys. Lett. **81**, 4055 (2002).

13. M.P. Taylor and H.D. Hallen, "Fabrication of Nanoscale Polymer Structures with In-Plane Molecular Orientation". Manuscript.

14. C.L. Jahncke and H.D. Hallen, J. Appl. Phys. Lett. **93**, 1274 (2003).

15. E. Betzig and J. Trautman, Science **257**, 189 (1992).

16. P. Pomorski, L. Pastewka, C. Roland, H. Guo, and J. Wang, Phys. Rev. Lett. B **69**, 115418 (2004).

17. P. Pomorski, C. Roland, H. Guo, and J. Wang, Phys. Rev. Lett. B **67**, 161404(R) (2003).

Chapter 2

2. Shear-force Feedback

2.1 Nonlinear Tip-Sample Interaction

Distance regulation in near-field optical microscopy (NSOM) makes use of the force interaction between the probe and sample. There are several experiments in which accurate distance control is essential: fluorescence lifetime, gradient field Raman, SSCM and electromigration [1, 2, 3, 4]. Understanding the dynamics of the probe interaction and the mechanism behind the distance control helps to optimize distance regulation and evaluate its accuracy. We find that a nonlinear interaction such as a tapping force is required to accurately describe the resonance behavior of the probe both in and out of feedback (near and far from the sample). Furthermore, our novel study of the system dynamics shows that the model is able to predict the detailed nature of the time response of the probe that we observe

in our measurements. Finally, we present strong evidence indicating that the probe is tapping on surface adlayers prior to tapping on the surface itself as the probe approaches the sample, and we comment on the suitability of shear-force feedback for accurate distance control.

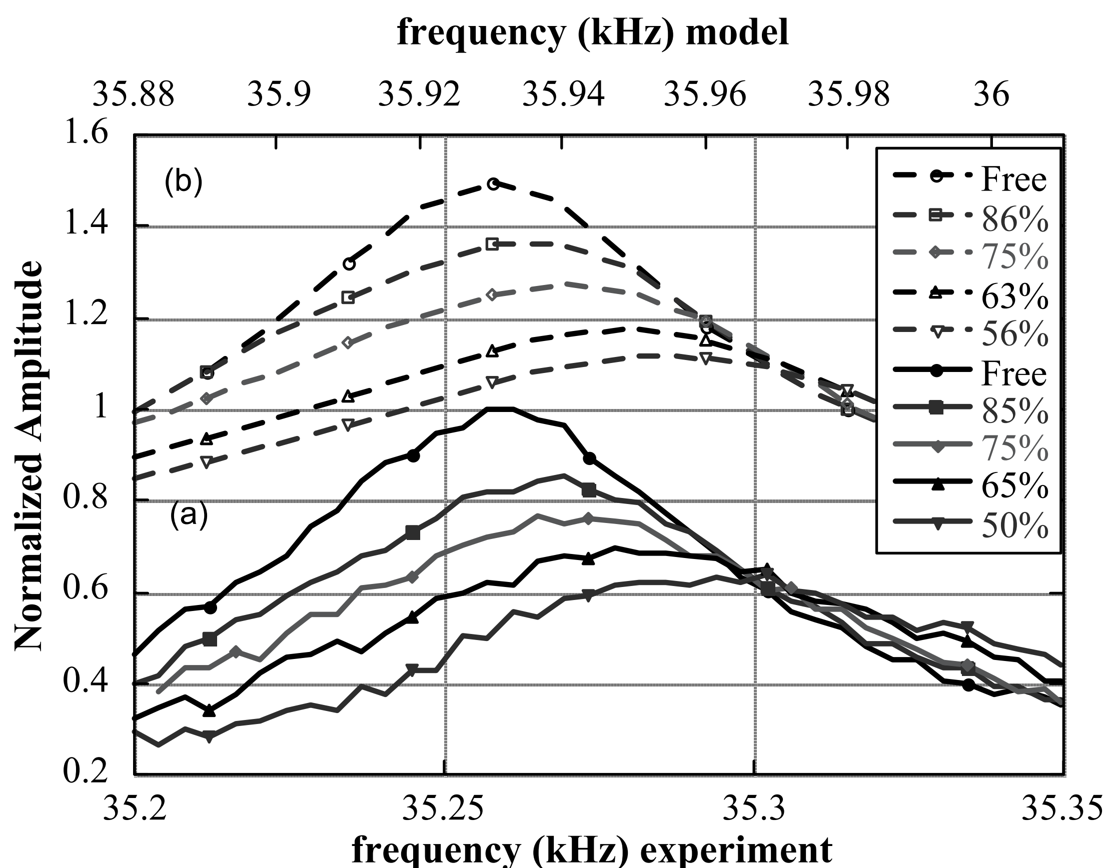

Figure 2. 1: (a) Typical resonance curves obtained with the tuning fork method of oscillation amplitude measurement at various tip-sample separations (solid lines). (b) Resonance curves with different degrees of tapping obtained by a numerical solution of the nonlinear differential equation.

Shear force feedback using a tuning fork oscillator is one of the most widely used techniques for controlling tip sample separation with NSOM [5]. It relies on voltage generation by a crystal tuning fork to measure the oscillation amplitude that varies with tip

sample distance. The oscillation amplitude decreases when the probe is close to the surface due to an increase in damping and a shift in the resonance frequency. A variety of mechanisms and combinations of mechanisms are proposed to be responsible for the interaction between the probe and the sample such as friction [6], tapping (or knocking)[7,8,9], distance dependent probe bending [10], damping layer [10-14], and coulomb fields [15]. In this dissertation we show evidence of a nonlinear tip-sample interaction. Of these mechanisms, only tapping and probe bending have a nonlinear response. Figure 2.1(a) shows the resonance curve far from the surface and its evolution as the probe is moved closer and closer to the surface. The resonance frequency shift seen implies that a nonlinear mechanism is active. The obvious nonlinear interaction is tapping.

To model this tapping interaction, we use a simple truncated driven harmonic oscillator used by others to model NSOM [7] and atomic force microscope [16] probe-sample interactions. In this model, the tapping force is included in the addition of a strong force when the lateral position of the tip exceeds a critical value, $\mathbf{x_c}$. The equation that describes such a system with effective mass m_{eff} driven by a force F_{drive} is

$$F_{drive}/m_{eff} = F_0\cos(\omega_d t)/m_{eff} = \ddot{x} + 2\beta_0\dot{x} + \omega_0^2\, x + H(x-x_c)[\, \omega_1^2\,(x-x_c) + 2\beta_1\dot{x}] \,, \qquad (1)$$

where ω_d is the radial tip oscillation driving frequency, β_0 and β_1 refer to damping and ω_0 and ω_1 the resonance frequencies of the fork/fiber oscillator and fiber/adlayer system, respectively, and H is the step function. We find ω_0 and β_0 from the free resonance curve. These parameters depend only on the tuning fork/probe assembly. From a combination of the

free resonance curve (H=0) and a shifted, damped resonance curve we determine ω_1 and β_1. We comment in more detail on the significance of the values of these two parameters for the physics of the tip-sample interaction later in the paper.

The parameter F_0/m_{eff} is used to normalize the equations so that the amplitude of x is 1 with no tapping (H=0). Numerical solutions to the model for various values of x_c give resonance curves as a function of the fraction of the undamped resonance peak (set-point) that are consistent with the resonance curves we find in our experiments (see Figure 2.1). Note that in both the numerical analysis and in the experiment, the damped resonance curve crosses over the free resonance curve on the high frequency side resulting in driving frequencies unavailable for normal feedback operation without switching the polarity of the feedback response.

We study the dynamics of the probe sample interaction by observing the calculated oscillation $x(t)$ as we add or remove the step function terms from the model. When we add the step function, we refer to the system as tapping on, and when we remove the step function, we refer to the system as tapping off. This is analogous to the probe being moved from a position out of feedback to a position close to the sample for the tapping on and vice versa for the tapping off. Figure 2.2(a) shows the time response of the model overlaid with the resonance curve. The time response becomes faster as we move off resonance in either direction, and the time response for turning the tapping off approaches the time response for turning the tapping on. At the resonance frequency, the time response for the tapping on versus off is very different.

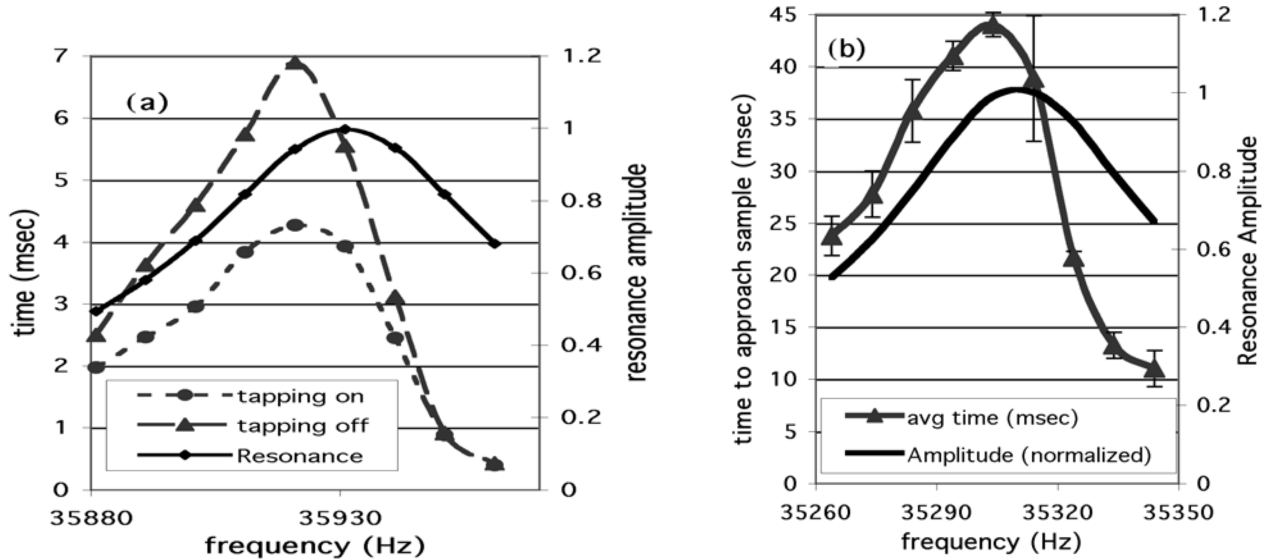

Figure 2. 2: (a) The numerical calculation of the time response for the feedback signal to drop to 1/e for a variety of driving frequencies for two situations: turning the tapping off and turning the tapping on. This time response is overlaid with the resonance curve for reference. (b) The experimental time response for the probe to find the surface with optimized gain given an 8msec-ramped trapezoidal step of height 30 nm.

The dynamic behavior of the probe predicted by the model is consistent with what we would expect qualitatively. Recall that there are two parameters responsible for the time response of the system when it is in feedback: the change in damping and the frequency shift, both can be seen in Figure 2.1. The time response is limited by the width of the resonance curve, in the sense that if the tip gets too far from the sample, the decay time for the oscillation scales inversely with the peak bandwidth. Thus the time response is slow due to the high quality factor (100 to 700) combined with the relatively low resonant frequency (32-40 kHz). When the probe is close to the sample, the oscillation decreases due to both the damping of the probe and the frequency shift, and while the damping is slow, the peak shift is fast. Near resonance, at probe positions relatively far from the sample, the slow damping

is dominant; at probe positions close to the sample, the fast peak shift is dominant. This inequity results in the two different curves for the cases of tapping on and tapping off. When the probe is off resonance, the peak shift is dominant, and the time response is faster for both cases.

In our experiments we clearly see the dynamic behavior predicted by the tapping model. Without lateral scanning, we apply a 30 nm trapezoidal shaped pulse with an 8 msec rise and fall time to the z-piezo, which ramps the tip alternately towards and away from the surface. The probe begins in feedback, so when it moves towards the surface, the tapping is increased (tapping on), and when it is pulled away from the surface, the tapping is decreased (tapping off). We maximize the gain until there is no overshoot when the probe retracts as a reaction to being pushed towards the surface. We plot the time response for the inward motion of the probe as a reaction to being pulled away from the surface as a function of driving frequency, and we see a behavior that is very similar to that predicted by the model, Figure 2.2(b).

In a second experiment to study the time response of the system, we apply a square wave to the z-piezo that moves the tip 40 nm alternately towards and away from the surface, while monitoring the system response. The feedback gain is the same for all frequencies. We expect the time for the system to respond when the pulse pushes the probe towards surface to be fast in all cases, pulling the probe away from the surface, due to the increased tapping. Since the gain is high, overshoot is observed when the 'ingoing' response is too slow. This will be the case without strong nonlinear effects (at frequencies near the

resonance peak). Figure 2.3 shows exactly this behavior. The curves shown are the in and out motion of the probe with the resonance curve overlaid for reference. As the pulse pulls the probe away from the surface, the time response for the inward motion, inversely proportional to the slope, decreases as we increase the driving frequency above the resonance peak until the time response for the in and out motion of the probe align. This balanced response quenches the overshoot. If this frequency rather than the peak frequency were used for feedback, the bandwidth of the NSOM (and SSCM) could be increased [17]. Further increases in frequency much beyond this point result in instability since the damped resonance curve begins to cross over the free resonance curve.

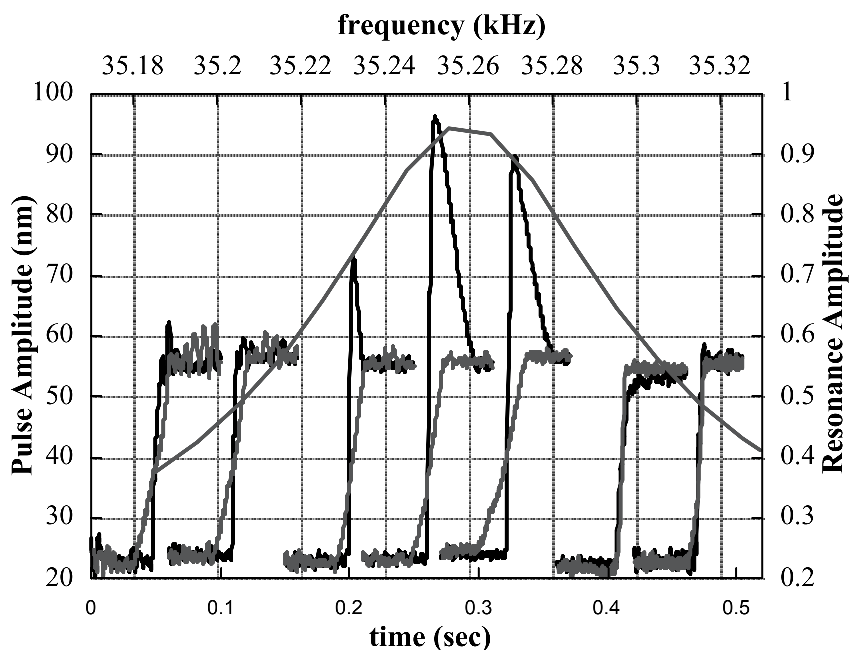

Figure 2. 3: The feedback response to an impulse of 40 nm on the z-piezo for a variety of driving frequencies on either side of the resonant frequency with constant gain. The black lines are the outward motion. The grey lines are the inward motion. The resonance curve is overlaid for reference.

With confidence in a model that accurately describes both the static and dynamic aspects of our system, we look more closely at the choice for ω_1 and β_1. Gregor uses the clamped resonance curve ($x_c = 0$) to determine these values, and they accurately describe the large frequency shifts and minimal additional damping of his resonance curves as the probe approaches the sample. Figure 2.4 shows several of our resonance curves including the

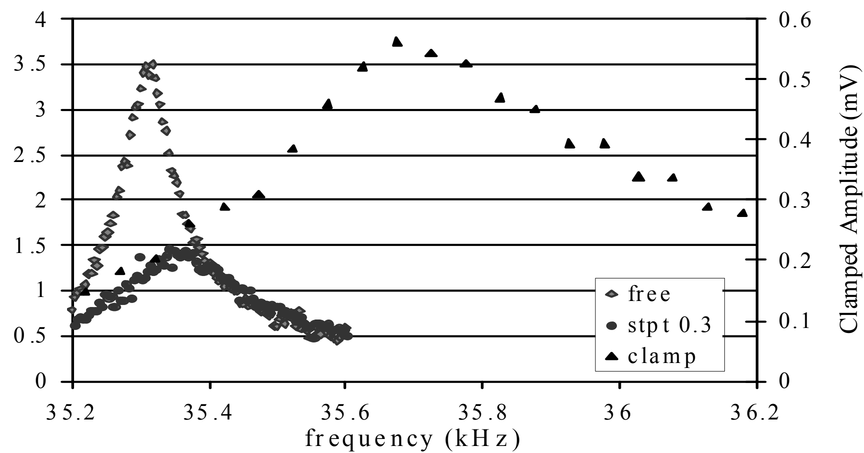

Figure 2. 4: Experimental resonance curves showing the undamped resonance, a resonance at 35% of the free resonance and a clamped resonance curve. The peak of the clamped resonance is only 2% of the undamped resonance peak, and the frequency shift is ~400Hz.

clamped curve. The trends are qualitatively different from Gregor's observation. We find that using the clamped curve to determine ω_1 provides values that give a poor fit to our data because the spring constant is too large. The frequency shift for the clamped peak is 400 Hz as compared to 60 Hz for the damped peak we use. A simple picture describes both our and Gregor's observations: for most of the approach curve, we are tapping on (soft) adlayers

compared to Gregor who is tapping on the sample surface or hard, frozen (low temperature NSOM) layers. Therefore, we must obtain the parameters for our model from the adsorbed layer tapping, not surface tapping if we are to describe the dynamics under normal ambient operation. We note that rather than tapping on the surface adlayers, the probe may be opening a cavitation hole within the adlayers, resulting in a tapping on the sidewalls of this cavitation hole. Near a hydrophilic surface, water is structured [18] as are other near-surface solvents [19], so they are less mobile, indicating that cavitation is likely with the ultrasonic tip oscillation frequency. Cavitation is also possible with less mobile adsorbates and the less structured water (clathrates) near a hydrophobic surface [20]. Either case, tapping on the adlayers or cavitating in them, is consistent with our observation of the change in stiffness that we observe when the probe reaches the sample surface.

If the probe is tapping on the sample surface, then the distance to the sample depends both on the fiber oscillation amplitude and the angle between the sample and the probe [9]. However, if the probe is tapping on surface adlayers, and the oscillation amplitude of the probe is much less than the thickness of the adlayer, then the distance to the sample depends primarily on the thickness of the adlayer and can be accurately controlled, as is the case with our system. In our studies, the tip does not tap on the hard sample surface (beneath the adlayers) in the normal operating range, or even closer to the surface, until the probe oscillation amplitude has decreased due to sample interaction to a few percent of the free oscillation value. This is clear from the small measured oscillation amplitude at the feedback

frequency (~1 nm) [17] compared to the 5-10 nm approach curve; the tip simply cannot reach the surface. As an additional evidence, in our electromigration studies[3,4] we have found that we cannot measure tunnel current between the tip and sample unless we set the feedback level much below the normal operating range (probe very close to the surface). The process is repeatable, with minimal tip wear determined by little change in resolution even after several hours at a low feedback level (tunneling). In the case of small probe oscillation amplitudes on surfaces with a contamination layer (typical case), shear-force is an accurate measure of probe-sample separation.

2.2 Data Analysis

In summary, the nonlinear model accurately describes both the system dynamics and the resonance curve behavior as the probe approaches the sample. During this approach the probe taps on surface adsorbed layers prior to tapping on the surface itself. This implies that the lateral force feedback is a good indicator of tip-sample distance when small oscillation amplitudes are used, and that a tapping mechanism describes the nonlinearity of the tip-sample interaction. This nonlinear interaction can be used to increase the bandwidth of the high Q tuning-fork-based distance regulation system; i.e. NSOM and SSCM.

2.3 Bibliography

1. X. Sunney Xie and Robert C. Dunn, Science **265**, 361 (1994).

2. E. J. Ayers, H.D. Hallen and C. L. Jahncke, Phys Rev Lett, **85**, 4180 (2000).

3. Suzanne Huerth, Michael Taylor, Michael Paesler and Hans Hallen, Proceedings of the Second Asia-Pacific Workshop on Near-field Optics, Beijing, China, (1999).

4. S. H. Huerth, M. P. Taylor, H. D. Hallen and B. H. Moeckly, Appl. Phys. Lett. 77, 2127 (2000).

5. Khaled Karrai and Robert D. Grober, Appl. Phys. Lett., **66**, 1842 (1995).

6. Lapshin, E.E. Kobylkin, V.S. Letokhov, Ultramicroscopy, **83**, 17 (2000).

7. M.J. Gregor, P.G. Blome, J. Schöfer and R.G. Ulbrich, Appl. Phys. Lett., **68**, 307 (1996).

8. I.I. Smolyaninov, W. A. Atia, A Pilevar, CC Davis, Ultramicroscopy, **71**, 177 (1998).

9. Kate Hsu and Levi A. Gheber, Rev. Sci. Inst., **70**, 3609 (1999).

10. P.K. Wei and W.S. Fann, J. Appl. Phys., **83**, 3461 (1998).

11. J. U. Schmidt, H. Bergander, and L. M. Eng, J. Appl. Phys., **87**, 3106 (2000).

12. P.K. Wei, W.S. Fann, J. Appl. Phys., **87**, 2561 (2000).

13. R. Brunner, O. Marti, and O. Hollricher, J. Appl. Phys, **86**, 7100 (1999).

14. Khaled Karrai and Ingo Tiemann, Phys. Rev. B, **62**, 13174 (2000).

15. C. Durkan, and I.V. Shvets, J. Appl Phys., **79**, 1219 (1996).

16. Michael Muto, M.S. Thesis, North Carolina State University, (1997).

17. C.L. Jahncke and H. D. Hallen, in press, J. Appl. Phys.

18. R. M. Pashley and J. A. Kitchener, J. Colloid and Interface Sci., **71**, 491 (1979).

19. R.G. Horn and J. Israelachvili, J. Chem. Phys., **75**, 1400 (1981).

20. P.M. Wiggins, Microbiol. Rev., **54**, 432 (1990).

Chapter 3

3. Imaging Techniques of Irregular Surfaces

3.1 Introductory NSOM

Paints are industrially important materials; quality control requires detection of the defect, and corrective action requires knowledge of the cause. To identify the defects, we propose nanometer to micrometer regime (mesoscale) optical and topographical surface characterization. In particular, a unique approach is presented for identifying and characterizing surface features through the use of NSOM. NSOM enables optical and topographical imaging of mesoscale surface features through high-resolution imaging [1, 2]. Light is input through a chemically etched, metal coated, fiber optic probe [3]; the probe is

brought within nanometers of a sample surface and rastered while the topographical and optical signal are simultaneously collected [4, 5]. The statistical analysis of these observations characterizes surface features such as clumping, pigment density fluctuations, and overall smoothness of sample surfaces. In addition, individual pigment particles can be identified. Two types of samples were imaged and defined as follows: a reference sample, R, of high quality and a low quality sample, N. The quality value is based upon visual inspection. This study of the samples shows that quality variations are differentiated at the mesoscopic length scales over which both the optical and topographic signals vary. A histogram of the variations shows a peak at a mesoscopic length for the R sample, while it continues to increase at smaller distances for the lower quality sample, N. Thus, the length scale of the fluctuations is more important for observing paint quality than actual fluctuations.

3.2 Imaging Methods

NSOM microscopes enable the extension of optical techniques for higher resolution imaging[5, 6]. In order to obtain high-resolution images, the system must be free of vibrational noise, the tip must be close to the sample, and stable feedback must be established [2]. In our system, shear-force feedback is the method of probe sample distance control [7, 8]. The NSOM setup uses a tuning fork oscillator to detect the tip oscillation amplitude and control the separation of the tip and sample [6]. Shear force feedback uses voltage generation by a quartz crystal tuning fork to measure the oscillation amplitude that varies with distance [7, 8]. Fiber probes (etched and metal coated) are carefully mounted with superglue to the side of the

tuning fork[9]. The tuning fork's resonance frequency is altered by the presence of the mounted probe [4]. The frequency changes from ~33 kHz to ~40 kHz due to stiffening of the mechanical oscillator (tuning fork and fiber). Once the probe is close to the sample surface, there is a change in resonance frequency and the oscillation amplitude decreases [1]. The nonlinear tapping interaction between the probe and layers adsorbed on the sample is used to increase the operational bandwidth of this high quality factor oscillation system [7]. To identify pigment distributions and individual particles, topographical and optical data were collected. For collection of topographical information, the optical probe raster scans across the specified scan range under z feedback collecting forward and backward data (in both directions) on the contour of the sample [6, 10]. The forward and backward images are correlated to insure artifact-free imaging and to determine noise levels [11]. For collection of optical data, a collection lens relays reflected light into a photomultiplier tube (PMT). Both the PMT and collection lens are located at a 45 degree angle to the sample surface normal. HeNe laser light (532.8nm) coupled into the optical probe is used for sample illumination. Both forward and backward optical images are correlated during analysis.

3.3 Imaging Results

Several areas on each of the reference and low quality sample were imaged and compared. The topographic images required background subtraction calculated from a least squares fit to a sub region of the image. It corrects for an overall tilt of the sample. Multiple images of ‘forward’ and ‘backward’ data for a particular image were analyzed and compared

to distinguish between artifacts and actual structures. Artifacts will not be repeated in both forward and backward data, but real features will [12, 13]. In analyzing forward and backward line cuts, a hysteresis is visible in the data due to inherent losses in the piezo-tube scanner during the lateral scanning process [14]. This phenomena is well identified and anticipated in these large scans, so it does not cause discrepancies in image analysis.

Figures 3.1 and 3.2 are images of the reference sample. Aligned, uniform circular structures can be seen, as expected from the reference sample. In Figure 3.2, it is possible to see the ridging of the polymer in the lower right corner of the image. The image scale ranges from white (highest point value) to black (lowest point value) with a distance range of 1920 nanometers, which is also the distance range for Figure 3.1. Similarities in the optical and topographical images indicate a coupling between topography and pigment distribution. Due to the large size scale and comparison of forward and backward images, we know that this is not a NSOM 'topographical artifact' but rather a real coupling between pigment density and topography [12, 15]. Knowing that we are able to resolve on a scale range near that of the pigment particles and identify what we believe to be the polymer structure, we focus on discriminating between the reference and low quality sample. We recorded and plotted the long and short term height variations in the two paint samples. Short term variations are defined as variations over a 300-500 nm length scale (one quarter the image size), and long term variations are defined as variations over the interval of the entire image range (1-2 μm). Overall, 62 images (optical and topographical) were evaluated for long and short term variations. All variations (long and short) are values averaged over three measurements. For

each long and short scale variation, two numbers were recorded; the first is the variation defined above and the second is the maximum average value in the image. The percent variations were obtained by dividing the first number by the second and multiplying by 100. The reason for normalization is to correct for variations of laser power or probe through-put in various images.

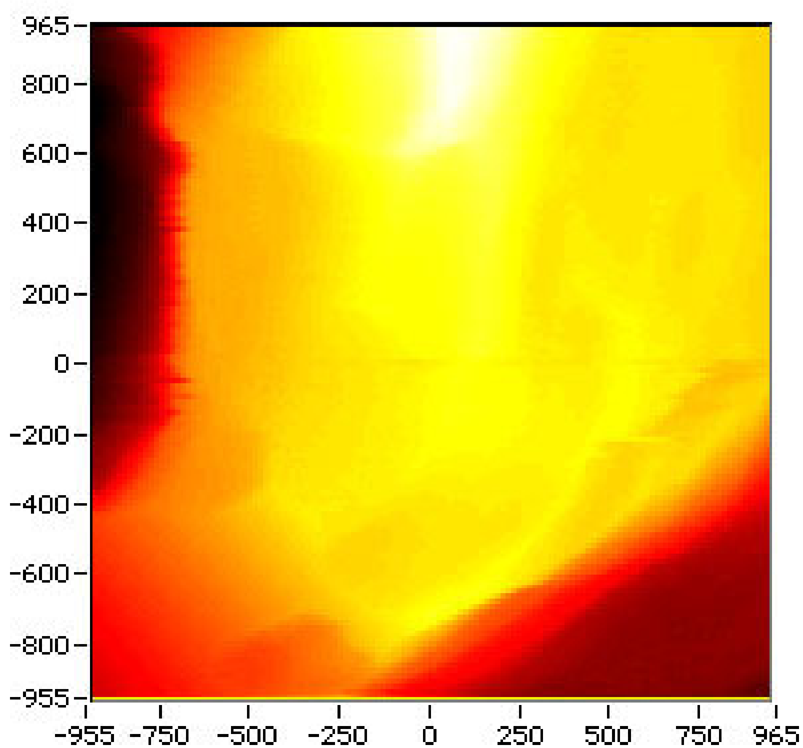

Figure 3. 1: This is a topographic scan of the reference sample (1905nm x 1905nm). The axes are in nanometers. The overall z distance range is 1138nm. The middle region of the image represents one plateau at a vertical position near 228nm. The upper middle portion of the image is 187nm above the middle plateau, and the bottom right where polymer ridging is observed is 663nm below the middle plateau.

The throughput is highly probe-dependent, and normalization allows quantitative comparisons of data from different probes. These ratios (long and short scale) were plotted and used to analyze the two paint samples. The low quality sample was imaged numerous

times showing pigment particles, but in non-uniform arrangements. There is no identifiable arrangement, but particle clumping was observed in Figure 3.3. From the histograms (Figure 3.4), we note the Reference, R, data are strongly peaked at low percent variation, whereas the low quality samples, N, show a much wider range in variation on all length scales ranging from very small variations (peak near zero) to large variations (beyond the peak of R).

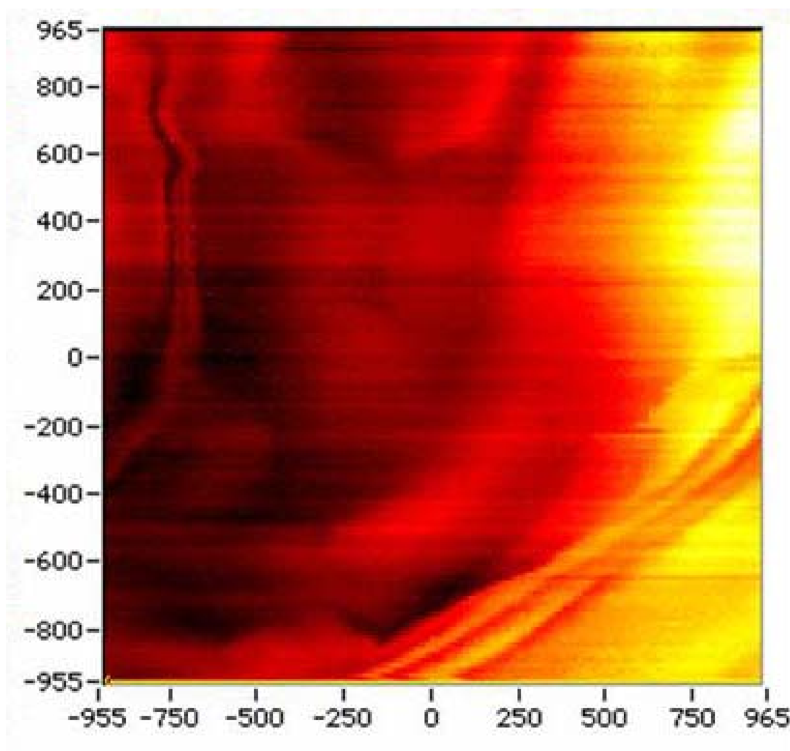

Figure 3. 2: This is an optical scan of the reference sample (1905nm x 1905nm). The optical range was measured in arbitrary units. The horizontal axis is in nanometers. There is an overall optical range of 0.051a.u. In the upper left and lower right portions of the image, polymer ridging is observed. This is consistent with Figure 3.1, which was taken over the same scan range.

That is, the Reference data are strongly peaked at a nonzero low variation, and drop sharply to zero, whereas the low quality samples decrease from a maximum near zero and exhibit a much longer tail. These mesoscopic traits distinguish the two paint samples.

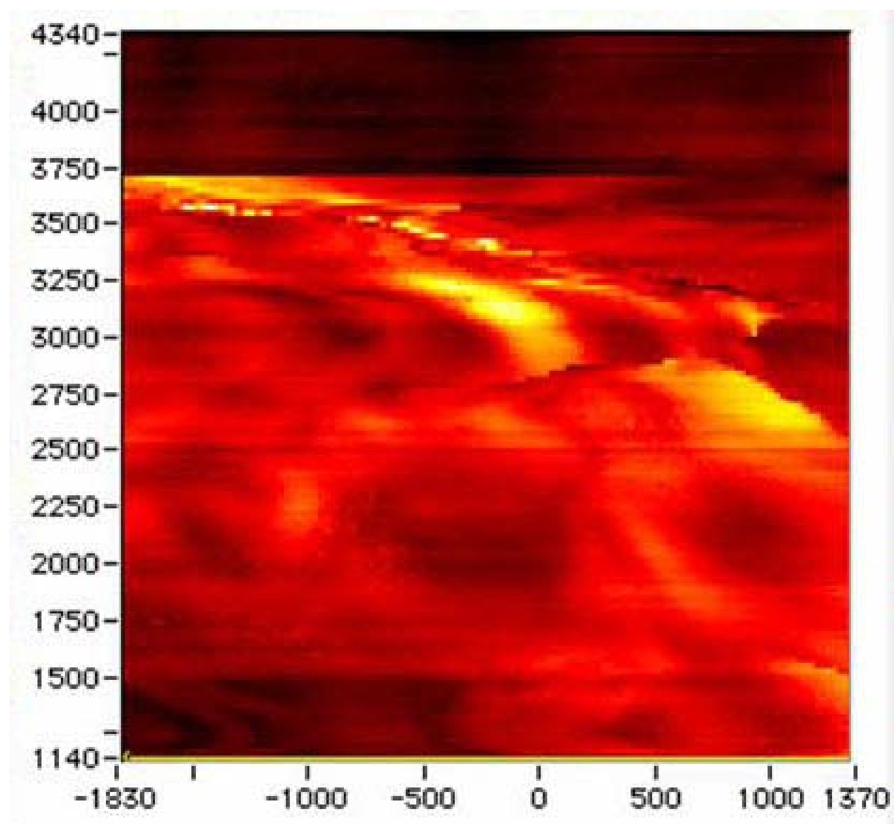

Figure 3. 3: This is an optical scan of the low quality sample (3175nm x 3175nm). The horizontal axis is in nanometers. There is an overall optical range of 0.27a.u. The scan shows pigment particle clumping in a non-uniform manner. Although the arrangement is non-uniform, it is still possible to identify pigment particles (see Figure 3.5).

3.4 Single Pigment Particle Imaging

Individual pigment particles were identified in several scans. Evidence of these single particles can be found in an image by expanding small regions of the images and scaling the color table, but is much more convincing in the forward and backward line cut

data. The line cut data allows us to look at z versus x or y, all measured in nanometers. It is free from color-table induced artifacts and elucidates the noise levels.

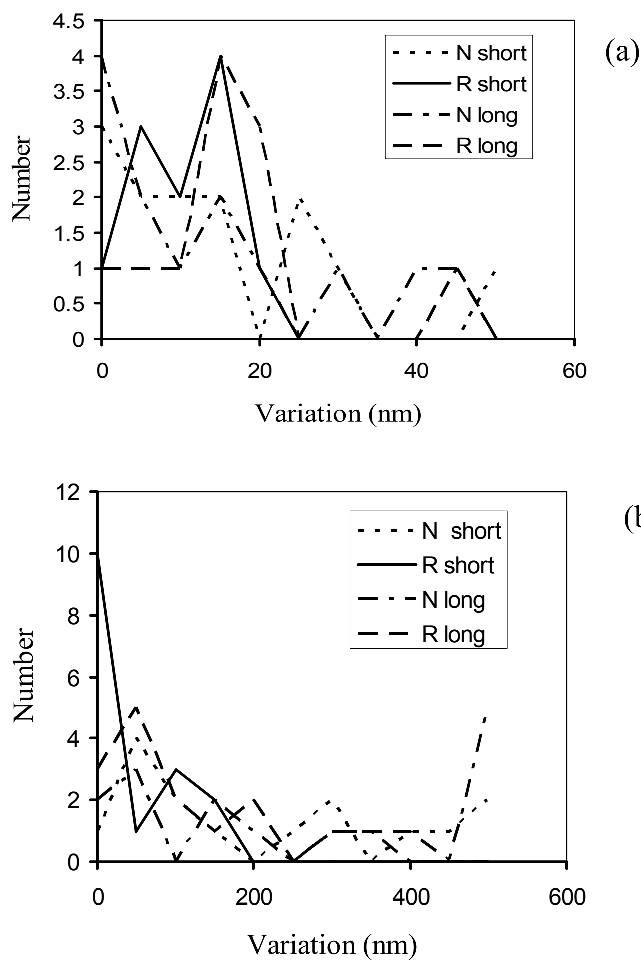

Figure 3. 4: (a) is a histogram of the optical variation and (b) a histogram of the topographical variation. In analyzing the percent variation, it is possible to distinguish between the reference and low quality sample.

Correlations of peaks in the forward and backward data of the optical and topographical scans permit identification of single pigment particles. The particles identified were 20-30 nm in half-height diameter, which is approximately our optical resolution. Figure 3.5 shows

the optical data in which arrows indicate the points that represent individual pigment particles, and we can identify the positions of various single particles that were resolved. There is a noticeable hysteresis in the forward and backward data which is due to lateral drift in the piezo-electric tube used for fine (x,y,z) adjustment [14]. The same particles were verified in the topographical data.

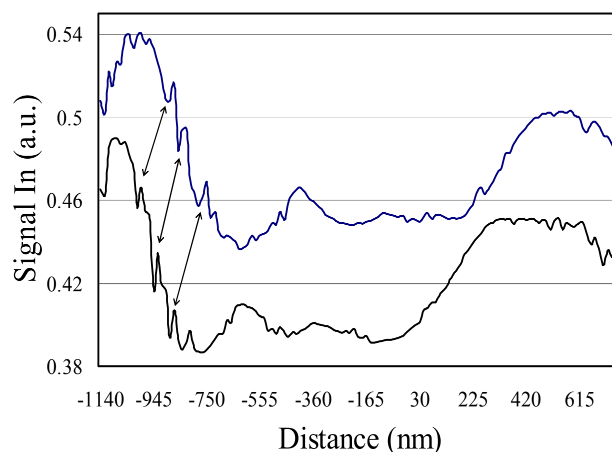

Figure 3. 5: This is the optical forward/backward line-cut data from the lower portion of Figure 3.3. The forward data have been shifted upward for clarity. The horizontal axis is distance (nm), and the vertical axis is in arbitrary units. The forward data (top graph) is shifted to the right of the back data (bottom graph) due to hysteresis. The arrows indicate corresponding data points in the forward and backward data that reflect the same pigment particles.

3.5 Data Analysis

Pigment particles near the sample surface were imaged with NSOM. Images of polymers in the paint sample also identified large scale structures such as ridged or clumped orientations. The scans of the low quality sample showed non-uniform arrangements of pigment particles

and also non-uniform particle clumping. Statistical analysis of paint sample images yields information about the mesoscale order of the pigment distributions. The histograms (Figure 3.4) illustrate our approach using the long and short term variations to distinguish between the low and high quality samples. The NSOM approach for sample identification and characterization was effective in allowing us to resolve features in the mesoscale regime, which distinguish high and low quality paints.

3.6 Bibliography

1. C.L. Jahncke and H. D. Hallen, J. Appl. Phys. **93**, 1274 (2003).

2. E. Betzig and J. Trautman, Science **257**, 189 (1992).

3. A. Lazerev, N. Fang, Q. Luo, and X. Zhang, Rev. of Sci. Instrum. **74**, 3679 (2003).

4. K. Karrai and R. Grober, Proceedings of SPIE, edited by Michael A. Paesler and Patrick J. Moyer 2535, 69 (1995).

5. R. Brunner, A. Bietsch, O. Hollricher, O. Marti, Rev. Sci. Instrum. **68**, 1769 (1997).

6. J. Hsu, Mat. Sci. Engin. **33**, 1 (2001).

7. C.L. Jahncke, S.H. Huerth, Beverly Clark III, and H.D. Hallen, Appl. Phys. Lett. **81**, 4055 (2002).

8. K. Karrai and R. Grober, Appl. Phys. Lett. **66**, 1842 (1995).

9. D. Davydov, K. Shelimov, T. Haslett, M Moskovits, Appl. Phys. Lett **76**, 1796 (1999).

10. M. A. Paesler, P.J. Moyer, Near-field Optics: Theory, Instrumentation, and Applications, Wiley & Sons (1996).

11. O. Fenwick, G. Latini, F. Cacialli, Synthetic Materials **147**, 171 (2004).

12. S. Bozhevolnyi, J. Opt. Soc. Amer. B **14**, 2254 (1997).

13. X. Wang, Z. Fan, T. Tang, J. Opt. Soc. Amer. A **22**, 2730 (2005).

14. D. Croft, G. Shed, S. Devasia, J. of Dyn. Syst., Meas., and Contr.**123**, 35 (2001).

15. B. Hect, H. Bielefeldt, Y. Inouye, D. Pohl, J. Appl. Phys. **81**, 2498 (1997).

Chapter 4

4. Novel Split-Tip Proximal Probe for SSCM and Fabrication of Nanometer-Textured, In-Plane Oriented Polymer Films

4.1 Introduction

Many complex materials, polymers, or molecular-based electronic devices depend upon the orientation of the components for their properties. This requirement places severe constraints on deposition techniques when lateral resolution on the nanometer length scale is required. We describe the fabrication of a scanning probe that can be used to deposit polymer molecules that are oriented in the plane of the surface[1]. This orientation is complementary to

self-assembled monolayers, SAMs, for which the orientation is perpendicular to the surface, and obviates the need for deposition of an electrode on top of the SAM polymer molecules. The latter process is difficult and often results in damage or destruction of the SAM due to the energy carried by the deposited species [2, 3]. The probe enables new device structures, since it can reverse the orientation of deposited, non-symmetric molecules with nanometer resolution. The result will be a potential barrier at the interface, which can be gated to provide device operation.

This dissertation presents the fabrication and electric connection methods of the central tool to enable this technique: the split-tip probe. It is built on a sharpened optical fiber. The fabrication process is not obvious; we show that methods developed for fabrication of near-field scanning optical microscope (NSOM) probes do not work well for fabrication of split-tips. The primary reason for failure is film stress and shorting problems. We model and demonstrate how these methods can be modified to successfully produce split-tips. The electrical connection to the probes is also difficult due to the requirement of multiple connections without shorting (to a thin film on a 125 micron diameter fiber), while simultaneously mounting the fiber for successful lateral force microscopy to allow the use of the split-tip on a scanning proximal probe microscope system. Another application of the probe is in Split-tip Scanning Capacitance Microscopy (SSCM), a novel electrical characterization tool in which the capacitance between the split-tip electrodes is measured. Additionally, information about the local sample conductivity is obtained (in a non-contact manner). The split-tip probe, which is mounted onto a standard scanning proximal probe

microscope, consists of two electrically isolated and independently contacted metal electrodes deposited on opposite sides of a tapered optical fiber, similar to those used for NSOM [4, 5]. An electron microscope image of a split-tip probe is shown in Figure 4.1. Aluminum (Al) or gold (Au) is used in these tips for electrodes and ultraviolet light confinement. A NSOM system has the required optical capability for coupling laser light down the fiber into the region between the split-tip electrodes, which is exactly where it is needed for initiating the deposition to the surface.

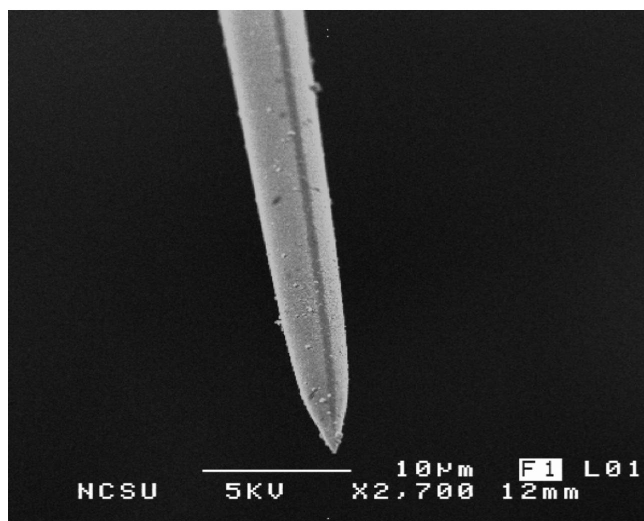

Figure 4. 1: The split-tip probe has electrodes on the left and right sides, and the aperture located at the bottom.

The probe not only guides the deposition, but can characterize the quality of the resulting material by the following: measurement of topography by the NSOM-like scanning probe [6], measurement of orientation with polarization-dependent NSOM imaging with the split-tip probe that is also used for deposition, and SSCM.

The key parameter for metal deposition is film stress. The most important factor for electrical isolation is the advantageous use of diffusion and island growth (Au) or oxidation (Al) in the regions between the electrodes. The major concern for mounting is that the thin film not be wiped off by the contact metal.

4.2 Probe Fabrication Methods

We first describe the oriented molecular deposition scheme used and some of the other criteria that impact the design of the probe, then detail the probe fabrication steps.

4.2.1 Probe Design Criteria

A schematic of the split-tip probe near the sample as molecules are being deposited with a fixed orientation to the sample surface is shown in Figure 4.2. In this cut-away view, the electrodes are on the left and right sides of the tip.

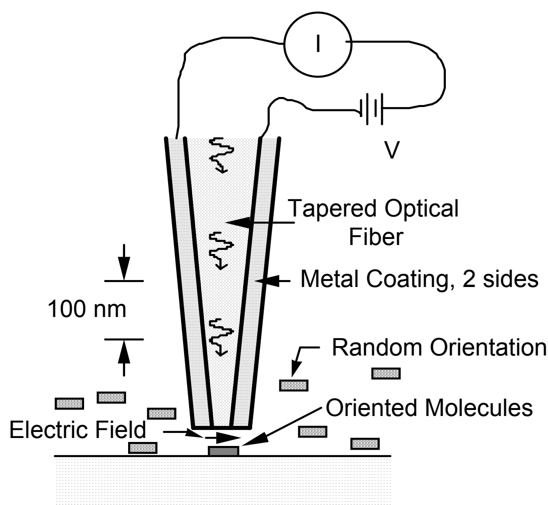

Figure 4. 2: Figure shows a schematic of the split-tip near the sample as molecules are deposited.

The electric field is localized in the region of the split, and is highest where the split is narrow (near the tip apex). Molecules that are in solution will be oriented and deposited where the field is high, but not elsewhere. When the tip moves to a new location, it aligns the molecules, then initiates the deposition to the sample with a pulse of ultraviolet light. The tip then moves to a new location, orients the molecules as they should be in the new location, and links them to the surface. It is important that molecules not under the probe aperture not attach to the surface, since they are not oriented. The scheme we have used is to spin a wet layer onto the surface, by exposing the regions for deposition while the molecules are rotated by the field, and then wash the remainder off. Another alternative is to load the tip with molecules as in the 'dip-pen' lithography scheme, oriented and attached as in liquid, then another molecule chosen for a different position [7]. These schemes have the same requirements for the probe. The requirements for the split-tip probe are as follows: the two electrodes must be electrically isolated from each other, the ultraviolet light must be able to propagate through the probe to the region between the electrodes, the deposition must not occur on the probe itself, the probe must be compatible with a microscope system, the probe must not be 'shorted' by the solution or the molecules that are in the solution, the probe must be usable in a probe-surface distance regulation scheme, and the probe should have a reasonable lifetime.

4.2.2 Probe Fabrication

The split-tip probe fabrication begins with sharpening an optical fiber using a process similar to that used for our NSOM tips. We have used either a Sutter Instruments puller,

modified to work better with fibers, [8, 9, 10, 11] or chemical etching [12] to taper the end of an optical fiber. Pulling fibers is needed when a large separation of the electrodes is desired, since the fiber gets a flat face as it cleaves in the fiber pulling apparatus, as can be seen in Figure 4.3. This shape contrasts with the sharp point (few nm radius) at the tip of properly etched fibers. Thus, if the electrodes are to be brought in close proximity of the surface, they need to be close together with etched fibers, but may be further apart when pulled fibers are used. Etched fibers are more reproducible to fabricate in large quantities, and have a higher optical throughput.

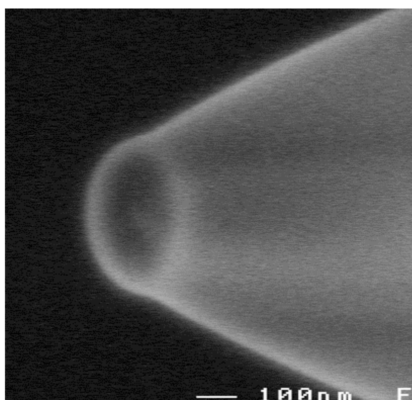

Figure 4. 3: SEM image of a larger-aperture tapered fiber fabricated by the heat-and-pull method. Note the flat cleaved end that is formed when this fabrication scheme is used, as opposed to the sharp point of etched fibers.

Once the fibers are shaped, metal is coated onto one side; then the fiber is rotated 180°, and the other electrode is deposited. This forms a split metal structure with the two metal sides electrically isolated. The metal coating must be thin (~5nm) so that the two sides do not short together. The probe-holding fixture mounts inside the deposition chamber, allowing an accurate flipping of the probes in vacuum and known orientation after removal

from the chamber. The probes are mounted on holders that keep the probes straight and separated by a sufficient distance to ensure they do not shadow each other during evaporation. Between 8 and 10 probes are held in each unit. Two units can be used at once in the evaporator system, oriented to face each other. The probe holder is mounted on a large gear, and the fiber tails run through a series of holders, also mounted on the gear, in the direction to prevent unraveling during rotation. The gear is turned by an electric motor. We have found that the motors work reliably in vacuum when they are driven by a voltage lower than their maximum rating. Although it is commonly known that the back-voltage generated by the motor limits the current and lower voltages result in motor over-current failure, we have found that the current is limited primarily by the resistance of the wires when these small motors are under load. Motor failures are usually the result of shorting from metal deposition or an increase in friction in the mechanism, often due to effects of metal deposition. Copper braiding connects the axle of the larger gear shaft to a liquid nitrogen cold trap mounted directly over the rotation units. In this way, the fibers can be cooled by radiation (with approximately pi-steradians of solid angle towards the cold trap) and by conduction through the copper braids, shaft, gear, holder, and fiber shanks. The evaporation chamber allows three different source materials to be used during one pump-down; Al and Au are commonly used for split-tips. Following the initial Al or Au deposition, a thicker coating (~100nm) of gold is applied to the contact regions on the shank of the tip. A small shutter, driven by an electric motor, is used to shield only the probe tips from the evaporation

source, so that the shanks are coated with metal. A close-up SEM view of the split-tip probe can be seen in Figure 4.1, and a view at higher magnification is given in Figure 4.4.

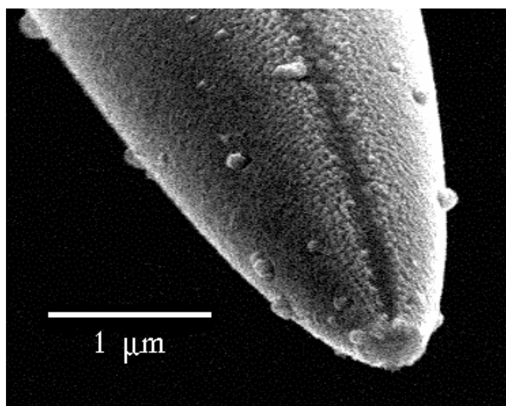

Figure 4. 4: The end of a split-tip fabrication with the optimal fabrication procedures.

4.2.3 Probe Mounting

The split-tip probe needs independent electrical contact to each side. Due to the concerns noted above, contact and lack of shorting between the two sides must be verified. Thus, two metal contacts are made to each side. Furthermore, the probe must be compatible with mounting into a scanning proximal probe microscope such as NSOM or SSCM systems. The latter entails mounting the probe tip onto the side of a quartz tuning fork (a few mm in length, with 32768 Hz free resonance) that is mounted to the microscope[5, 13]. To prevent shear from removing the metal layer near the contacts, the fiber must be held securely in place, without translation or rotation. Our system allows for these constraints by rigidly holding the fiber in a V-groove/clamp with 2 gold wires pressed against each side. This is shown in Figure 4.5. A Teflon holder is held to a glass plate by a spring guided by Sapphire

hemispheres attached to the bottom of the glass plate. The V-groove allows the s plit-tip probe to rest securely keeping the lower electrode of the probe positioned on the metal contacts.

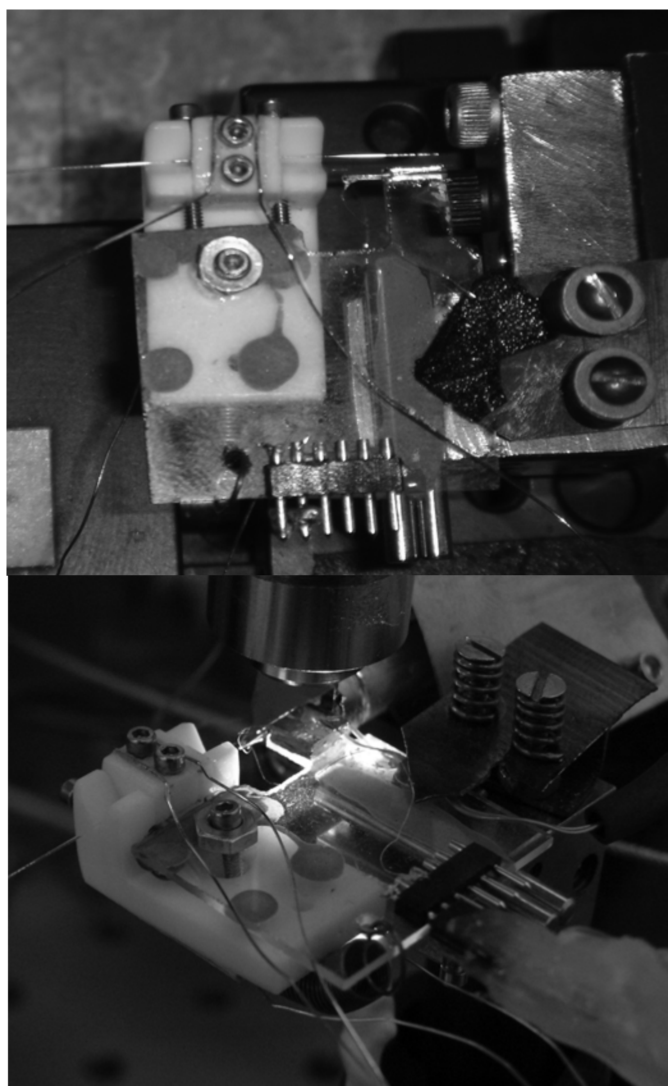

Figure 4. 5: A photograph of the tip holder; a piece of glass shaped to hold the tip on a tuning fork (upper right portion), the Teflon holder on the upper left keeps the gold wires positioned for contact with the fiber. The fiber can be seen passing through the groove in the Teflon where it contacts the wires, and on to the tuning fork (partially hidden).

There is an additional Teflon cover secured by screws providing contacts to the top split-tip electrode. This Teflon fixture can be translated and rotated with three screws to bring the fiber probe up against the tuning fork. Both the fixture and tuning fork are mounted to a glass plate (Figure 4.5) that fits onto the scanning probe microscope, so that mounting can be performed conveniently away from the scanning probe microscope, under a dissection microscope. Once the probe is against the tuning fork, glue is applied to the joint and the adjustments left fixed. A drop of epoxy applied to the base of the tuning fork improves stability.

We have found that the clamping of the fiber as shown in Figure 4.5 does not impair the lateral force microscopy as used in NSOM [13]. Also, there have been no observed significant differences in the resonance behavior of the split-tips compared to uncoated or uniformly-coated NSOM probes.

4.2.4 Probe Usage

The operating sequence once the probe is mounted begins with verifying that contact is established on both sides by measuring the resistance between the wires on the same side of the probe with a multimeter. When both sides have contact, the resistance between the two sides is measured, and should be too large for the meter to register. Possible causes of a lower resistance include a twisting of the probe so that the split is shorted at the contact wires, or a probe short near the tip, formed during the deposition of the metal. The latter typically occurs when there is an etching defect that leaves a mound or hollow on the taper near the aperture. The geometry of the mound is such that metal can coat across the split on

the edge of the mound. Shorting can happen if Al probes are not sufficiently oxidized. It is possible to measure the resistance from one wire on the holder to the fiber coating itself, by using a thin (0.002 inch diameter) gold wire to make the contact to the coating. However, this contact is not as reliable as a fixed contact. Once the electrical characteristics of the probe and connections are verified, a variable voltage is applied to the probe. We sometimes replace the ground lead with the virtual ground of a high gain current preamplifier, to monitor the magnitude of any shorting current as a more discriminating detector of shorts.

4.3 Results & Discussion

A significant challenge in the fabrication process is the production of a well defined split and a smooth continuous coating of metal all the way to the aperture of the probe. This is much less difficult for NSOM probes since the metal forms a continuous ring around the diameter of the NSOM probe. If there is stress in the metal layer, the film itself will hold the stress. When the metal is thermally evaporated, the stress is typically tensile [14]. This means that the metal will try to pull itself apart from the probe. If the metal is continuous, it will pull on itself, and usually remain stable. On the split tip, the metal is not continuous; so the stress must be held by the interface between the film and the underlying silica. Far from the tip, this is possible since the area is large; but as the tip is approached, the area is reduced and the curvature increased. The series of SEM micrographs in Figure 4.6 illustrate this. There appears to be a near perfect split in our split tip at low magnification, Figure 4.6(a). It is crucial to see this type of behavior at the aperture of the probe, rather than up the shaft.

Approaching the probe aperture, at 2000 times magnification, Figure 4.6(b), shows cracking and peeling, which presents a significant problem. Figure 4.6(c) shows the probe at 11,000 times magnification, clearly indicating problems with tensile stress [15, 16]. The aluminum film on the right side of the split tends to bow in a few regions. It is also seen from this micrograph that tensile stress will relieve itself through micro cracking of the film and peeling of the cracked surface from the substrate. The stress distribution in this film is anisotropic; cracking patterns depend on the stress distribution.

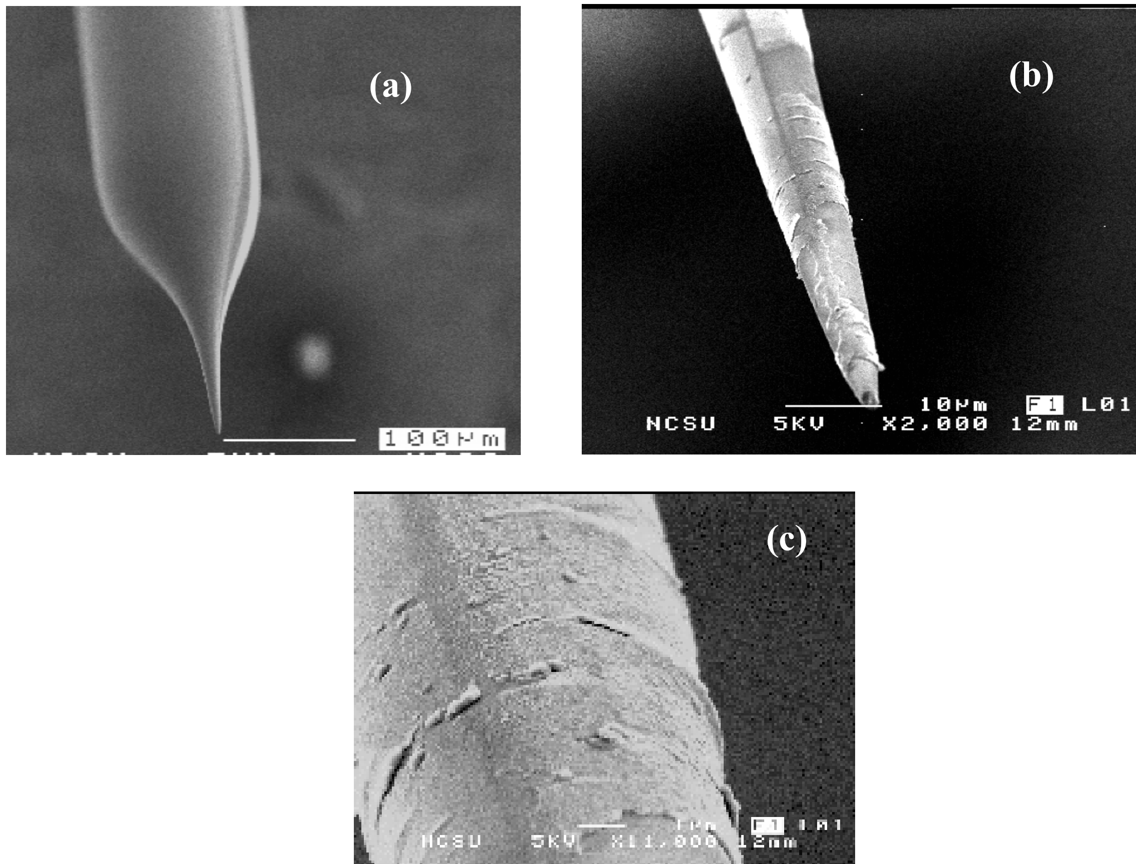

Figure 4. 6: (a) shows split-tip probe fabricated with certain imperfections, such as voids in the coating. (b) shows cracking and peeling which presents a significant problem. (c) shows tensile stress.

Thermal stress, due to difference of thermal expansion of the coating (Al) and substrate (sharpened silica fiber), is accentuated by the small volume of substrate at the tip. This small thermal mass allows large temperature changes due to the energy carried by the metal atoms impinging on the surface. Upon cooling from the deposition temperature to room temperature, the difference in thermal expansion coefficients of the substrate and the film causes thermal stress. The curling of the metal layer near the aperture, along with the observed cracking of the probe coating is due to stress in the coating (a thin film of Al) caused by differences in thermal expansion (thermal stress) between the Al and the silica fiber. The most common way for measuring film stress is by measuring the deflection (bowing) of a thin film substrate (beam or disc) on which the film has been deposited. This is not possible here, due to the shape of the substrate. The substrate is coated on both sides, and hence no bowing is expected or observed.

The temperature change at the tip during deposition can be estimated with a simple calculation. The first process that can contribute to probe heating is energy deposited by the metal evaporant,

$$\text{Energy Input} = Rc\rho\Delta TA\cos(\theta+\psi), \text{ with } A = 2\pi z\, dz/\cos\psi\ \tan\psi, \qquad (1)$$

where the factors are the evaporation rate $R = 1$ nm/s that would be obtained onto a flat, untilted surface the same distance from the source as the tip, an angle correction $\cos(\theta+\psi)$ for the tip with half-angle $\psi=6°$ tilted up at angle $\theta = 45°$, the heat capacity $c = 400$ J/kg/K for Al, density $\rho = 2700$ kg/m^3, temperature change of the evaporant as it cools $\Delta T = 800$ K

above ambient, and area of the film A at distance z from the tip. The second process that can heat the tip is radiation from the thermal evaporation source. Radiative heating power is given by $P = \sigma\varepsilon A(T^4 - T_o^4)(SA)$, which is proportional to the area A and solid angle SA. The emissivity ε is approximately 0.06 for shiny aluminum and 0.80 for the glass fiber. The transition will take place in the first few nanometers of deposition. For a temperature of 930K and solid angle of $SA \sim 10^{-5}$, the contribution from radiative heating into the same area as for evaporation is about an order of magnitude smaller than the deposited metal energy. Both have the same area factor and will enter the equations similarly. Radiative cooling is small despite the larger solid angle because of low emissivity and a smaller temperature difference. Cooling is primarily by conduction up the fiber taper, as determined by:

$$\nabla^2 T - \frac{\rho c}{\kappa}\frac{dT}{dt} = \frac{Q}{K}, \qquad (2)$$

where κ =1.5 W/m/K is the thermal conductivity of quartz, ρ the density, c the heat capacity, and Q the thermal energy per volume. Although an effective κ could be used to account for additional thermal conduction by the metal film, the total metal thickness here is too small to create a significant difference [17]. In steady state, the time derivative vanishes. Since the taper is a cone to a good approximation, and given the symmetry and a lack of significant radiation (and no convection), it is possible to convert the thermal problem to one of spherical symmetry, with the energy input per volume given by that in equation (1) scaled by the inverse of the fraction of solid angle taken by one tapered fiber: $2/(1-\cos\psi)$. This assumes that the energy is uniformly input rather than at the sides of the taper, but is justified

by the relatively shorter lateral thermal times. The energy input in (1) is divided by the volume of a shell at a radius z to get

$$\frac{Q}{\kappa} = \frac{RrcDT\cos(\theta+\psi)}{\kappa(1-\cos\psi)\cos\psi\tan\psi}\frac{1}{z} = D\frac{1}{z} = 633K/m\frac{1}{z}. \quad (3)$$

Equation (3) in spherical coordinates becomes, for steady state and uniform angle,

$$\frac{1}{z^2}\partial_z(z^2\partial_z T) = \frac{Q}{\kappa}. \quad (4)$$

This is solved by a function of the form T = A/z + B + Cz. The derivative is set equal to zero at the end of the taper L (0.5 mm) to indicate the reduction in heat flow at the end of the cone, and the temperature is set at the end of the taper to ambient, T_0. This implies

$$T = DL^2/2\,(1/z) + T_0 - DL + D/2\,z. \quad (5)$$

Near the end of the fiber, the last 2 terms are small; and at z = 1 micron, the temperature rise is ~150 K above T_0.

When the liquid nitrogen is cooled in the cold trap, the temperature of the fiber holder T_0 decreases to between 120K and 150K below ambient. Thus, the region near the probe aperture during evaporation is at or reasonably close to room temperature during evaporation. This is required to minimize thermally induced stress.

The following steps are used for fabricating the probes:

1. Cooling the tips as described in the paragraphs above.
2. Depositing a very thin aluminum film near the tip, on the order of 5-10 nm.
3. Applying a thicker coating (100-200nm) of gold to the contact pads so that they will be reliable under repeated use.

Tensile stress by is reduced by coating in multiple steps, with a 2-3 minute cooling period allowed between each step. The stress is also reduced by avoiding a large value for the film thickness, which further reduces the potential for shorting, discussed below. The substrate-film heating is also minimized, since the deposition duration is short. However, it results in a partly oxidized Al layer unless the vacuum is very good. These steps minimize the thermal stress by keeping the tip as close as possible to room temperature during the deposition through cooling and reduced thermal input. The stress is less important for the contacts, since they are in the region where the fiber is its full cylindrical radius, having larger overlap area to support stress and sufficient thermal mass to prevent significant thermal variation.

Figure 4. 7: Figure shows a detailed view of the separation between the split-tip electrodes. The split is not completely void, containing small grains of material.

The result yields well defined 'split' behavior in the probes with no sign of stress relief previously observed. At greater magnifications (Figure 4.7), it is possible to observe the detailed features of the aperture displaying the consistency and control of both the split and the deposition of the material used (Al).

Mathematically, a perfectly-aligned deposition from a point evaporation source will uniformly approach zero at the point where the probe surface is perpendicular to the evaporation source. The effect is most dramatic very near the tip, where the distances involved are short. Figure 4.7 provides a detailed view of the split. The split is, in fact, not completely void, but contains small grains of material. The grains are sparse within the split and vary in size from a few nanometers to tens of nanometers. The fact that the material is sparse and composed of 'balls' and individual grains (not a relatively smooth coating) is likely due to Ostwald Ripening or coarsening [15, 16]. The metal nucleates as small, dispersed particles initially, but the smaller particles slowly disappear as materials 'evaporate' onto a few that grow relatively large. This spontaneous diffusion process occurs because large particles are more energetically favored than smaller ones, and is well known for gold. The thicker film is more stable, so the transition causes the well-defined split edges to form.

Another factor that improves the electrical isolation is oxidation. Very thin metal within the split will be completely oxidized (if aluminum is used). This can be enhanced by exposing the probes to a few hundred mTorr of pure oxygen for ½ hour as a preliminary step to venting the system. This process is followed with all aluminum-deposited probes.

4.4 Data Analysis

In this chapter, the design and fabrication of a novel split-tip probe is presented. The split-tip probe has multiple applications including deposition of in-plane orientated nano-patterned molecules, characterization, and split-tip scanning capacitance microscopy

(SSCM). The probe mounts into and expands the versatility of conventional scanning probe microscopy such as NSOM and SSCM. The fabrication is significantly more difficult than standard NSOM probes due to the inherent unstable nature of the 'small metal plates' that form the split-tip. Theoretical models of the heating during evaporation help to design a method for the fabrication of low stress films required in this unusual deposition geometry. A mounting scheme to reliably contact the probe, while allowing the probe to be used in a scanning probe instrument, is described. The fabricated probes perform well in topographic and optical microscopy in addition to the unique functions enabled by the split-tip.

4.5 Bibliography

1. M. P. Taylor and H.D. Hallen, “Fabrication of Nanoscale Polymer Structures with In-Plane Molecular Orientation”. Unpublished.
2. Z. Zhu, D.L.Allara, N. Winograd, Appl. Surf. Sci. **252**, 6686 (2006).
3. E. A. Speets, P. T. Riele, M. A. F. Van Den Boogaart, L. M Doeswijk, B. Jan Ravoo, G. Rijnders, J. Brugger, D. N.Reinhoudt, D. Blank, Adv. Funct. Mat. **16**,1337 (2006).
4. C.L. Jahncke and H.D. Hallen, J. Appl. Phys **93**, 1274 (2003).
5. E. Betzig and J. Trautman, Science **257**, 189 (1992).
6. B. Clark III, G. Gurguis and H.D. Hallen, J. Vac. Sci. Tech. B **1**, 54 (2007).
7. R.D. Piner, J. Zhu, F. Xu, S. Hong and C.A. Mirkin, ""Dip-Pen" Nanolithography," Science **283**, 661 (1999).
8. B.I. Yakobson, P.J. Moyer and M.A. Paesler, J. Appl. Phys. **73**, 7984 (1993).
9. R.L. Williamson and M.J. Miles, J. Appl. Phys **80**, 4804 (1996).
10. Mufei Xiao J. Vac. Sci. Tech. B **15**, 1516 (1997).
11. G.A. Valaskovic, M. Holton and G.H. Morrison, Appl. Opt. **34**, 1215 (1995).
12. P. Hoffmann, B. Dutoit and R.P. Salathé, Ultramicroscopy **61**, 165 (1995).
13. C.L. Jahncke, S.H. Huerth, B. Clark III, and H.D. Hallen, Appl. Phys. Lett. **81**, 4055 (2002).
14. H. Murbach and H. Wilman, Proc. Phys. Soc. B **66**, 905 (1953).
15. L. Nedkov, T. Merodiiska, L. Slavov, R. Vandenberghe, Y. Kusano and J. Takada, J. Magnetism and Magnetic Mat. **300**, 358 (2006).
16. L. Lucchetti, L. Gobbi and F. Simoni, Molecular Crystals and Liquid Crystals **359**, 89 (2001).

17. A. La Rosa, B. I. Yakobson, and H.D. Hallen, Appl. Phys. Lett. **67**, 2597 (1995).

Chapter 5

5. Split-Tip Scanning Capacitance Microscopy (SSCM): A Finite Element Model

5.1 Introductory Modeling

Standard Near-field Scanning Optical Microscopy (NSOM) setups provide various means of high-resolution imaging [1, 2]. Optical and topographical imaging of surfaces has been the standard for many years [3, 4, 5]. Other properties measured include polarization, stress, and Raman Spectroscopy. Light is input through a chemically etched and metal coated probe. The sample's surface is rastered while the topographical and optical signals

are simultaneously collected [6, 7]. Here we describe the use of a novel split-tip probe as a means of electrical characterization of surfaces with nanoscale resolution. This additional imaging component has been added to the standard NSOM configuration. The metal probe used has been modified; rather than rotate the probe for uniform metal deposition, metal is evaporated onto opposite sides to create the probe. A combination of shadowing, diffusion, and oxidation yields a probe with two electrically isolated electrodes, a 'split-tip'. The production and fabrication of this slit-tip probe is discussed in detail elsewhere. In essence, a probe with two independent electrodes is created; each probe acting as a capacitor plate. The optical NSOM source is between the plates, so electro-optical effects can be studied at the nanoscale level.

As with any new technique, the study presented here examines the relation between the split-tip probe and sample surface to determine the accuracy and utility of capacitance measurements from the sample. The new measurements are correlated by topography and optical data through simultaneous, conventional NSOM techniques [8, 9]. We call this aggregated data collection method Split-tip Scanning Capacitance Microscopy (SSCM). The SSCM setup includes topographic and optical scanning techniques, but in this dissertation we focus on the measurements obtained through approach capacitance scans [10, 11]. The process for collecting capacitance data is the same as conventional NSOM. The sample will be rastered at appropriate distances from the split-tip probe, and the capacitance signal will be measured [12, 13, 14].

A finite element model has been developed that measures capacitance values given the tip-sample setup described previously. The model is created including a split-tip probe and a sample (here using samples with various material properties). Appropriate boundary conditions are established, and values of capacitance are measured at various distances from the probe to the sample surface. Finally the sample is theoretically revisited, with these steps repeated for each image point.

5.2 Model Methods

In order to make a solvable split-tip model, the system and boundary conditions must be specified. Noting $\partial t \equiv (\partial / \partial t)$ the following equations govern the model:

$$\nabla \times \mathbf{E} = -\partial t\, \mathbf{B}, \tag{1}$$

$$\nabla \times \mathbf{H} = \mathbf{J} + \partial t\, \mathbf{D}, \tag{2}$$

$\nabla \cdot \mathbf{D} = \rho$, with $\mathbf{D} = \varepsilon\, \mathbf{E}$, and ρ defined as the charge density and for metals, the surface charge (σ) is defined as the ratio of total charge to area

$$\sigma = Q/A, \tag{3}$$

$$\nabla \cdot \mathbf{B} = 0. \tag{4}$$

Defining **n** as the normal vector in a linear dielectric,

$$\varepsilon \mathbf{E} \cdot \mathbf{n} = \sigma, \tag{5}$$

where ε is the dielectric constant.

Given electric fields and potentials have a linear relation to source charges, super position can be exploited to develop a set of linear equations that define the split-tip system [11,13]. When charges are placed on all conductors in the system, the following expression can be used to express the charges as a function of the potentials [13]:

$$Q_i = \sum_{j=1}^{n} C_{ij} \Delta V_j \, , \tag{6}$$

where ΔV_j is defined as $V_i - V_j$ and C_{ij} represents the coefficients of capacitance. Each conducting surface (Figure 5.1) is represented by a capacitance coefficient and is calculated. More specifically, each coefficient is expressed in matrix notation

$$\begin{vmatrix} Q_1 \\ Q_2 \\ Q_3 \\ Q_4 \\ Q_5 \end{vmatrix} = \begin{vmatrix} C_{11} & C_{12} & C_{13} & C_{14} & C_{15} \\ C_{21} & C_{22} & C_{23} & C_{24} & C_{25} \\ C_{31} & C_{32} & C_{33} & C_{34} & C_{35} \\ C_{41} & C_{42} & C_{43} & C_{44} & C_{45} \\ C_{51} & C_{52} & C_{53} & C_{54} & C_{55} \end{vmatrix} \begin{vmatrix} \Delta V_1 \\ \Delta V_2 \\ \Delta V_3 \\ \Delta V_4 \\ \Delta V_5 \end{vmatrix} , \tag{7}$$

where the matrix is symmetric, i.e., $C_{21} = C_{12}$, etc.

From the model boundary conditions and Equation 7, the individual capacitance values are calculated providing the split-tip capacitance values.

In this chapter, we present three cases for study:

- lateral capacitance scans with the split aligned parallel and perpendicular to nanorod
- approach capacitance scans of aluminum and silica
- dopant density scans for different conductivity settings.

5.2.1 Lateral Capacitance Scans

Figure 5.1 shows an image of the finite element model that is developed to describe the split-tip system. The split tip probes are azimuthally oriented about the y axis. The rod and substrate are both oriented parallel to the z axis. Lateral scans simulate the 'rastar' scanning process used in SSCM and other scanning probe techniques. The split-tip probe rastars with the split aligned perpendicular to the nanorod and substrate [5, 7, 8]. Figure 5.2 shows the lateral scans mode with the split aligned parallel with the nanorod and substrate.

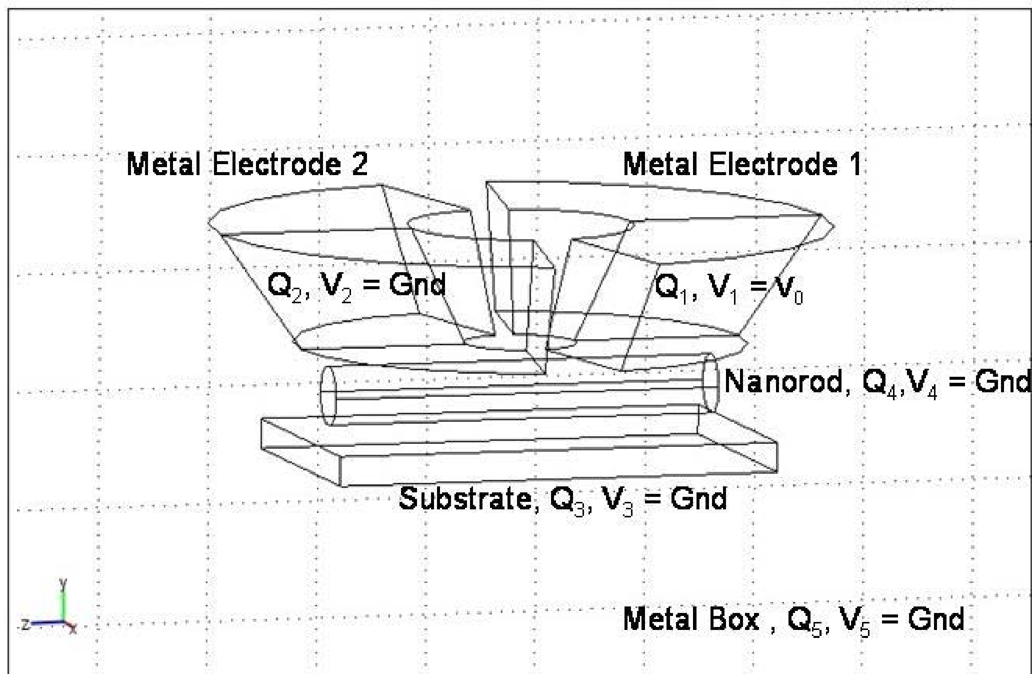

Figure 5. 1: Image of the split-tip probe positioned over a nanorod and substrate. The split is perpendicular to the rod and substrate.

The model consists of the aluminum coated split-tip probe with 30nm metal thickness (measured from bottom), a 70nm rod with 5nm radius, a 50nm by 80nm substrate, and a $1000nm^3$ metal box for shielding. The finite element calculation (Femlab) is influenced by the shielded box and affects the results due to the asymmetric positioning of the split-tip during the rastar scan.

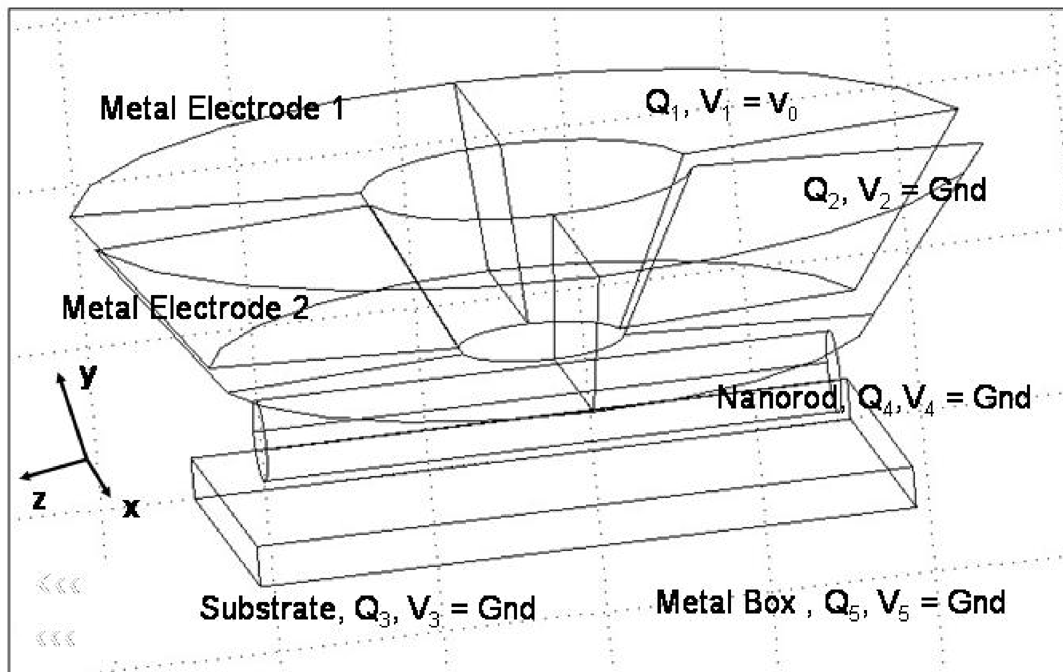

Figure 5. 2: Split tip rotated about y axis by 90 degrees.

Box size was increased until the asymmetric impact was minimized. Electrode 1 has a potential V_0 while the other four surfaces are grounded. Thus all the ΔV 's not relative to electrode 1 are zero. Given there are five conducting surfaces, Equation 6 becomes

$$Q_i = \sum_{j=1}^{5} C_{ij} \Delta V_j . \tag{8}$$

With model boundary conditions, Equation 8 yields the following set of linear equations:

a. $Q_1 = (C_{12} + C_{13} + C_{14} + C_{15})(\Delta V_2)$, where $\Delta V_2 = \Delta V_3 = \Delta V_4 = \Delta V_5$ and $\Delta V_1 = 0$

b. $Q_2 = (C_{21})(\Delta V_1)$, where $\Delta V_2 = \Delta V_3 = \Delta V_4 = \Delta V_5 = 0$

c. $Q_3 = (C_{31})(\Delta V_1)$, where $\Delta V_2 = \Delta V_3 = \Delta V_4 = \Delta V_5 = 0$ (9)

d. $Q_4 = (C_{41})(\Delta V_1)$, where $\Delta V_2 = \Delta V_3 = \Delta V_4 = \Delta V_5 = 0$

e. $Q_5 = (C_{51})(\Delta V_1)$, where $\Delta V_2 = \Delta V_3 = \Delta V_4 = \Delta V_5 = 0$

Equation set 9 can be solved for the respective capacitances. In particular the capacitance between the split-tip electrodes (C_{21}) is of interest noting $C_{12} = C_{21}$. It is this capacitance that we seek to plot in the lateral and approach capacitance scans.

5.2.2 Approach Capacitance Scans

Approach capacitance scans are taken for an aluminum and silica substrate. The model properties are set to simulate an aluminum or silica material respectively. Figure 5.3 shows the configuration of the model for approach capacitance scans. The rod has been removed, and the distance (in the +/- y direction) between the split-tip and sample is varied while the capacitance is measured. Now Equation 8 becomes

$$Q_i = \sum_{j=1}^{4} C_{ij} \Delta V_j \,, \tag{10}$$

yielding the following set of linear equations:

a. $Q_1 = (C_{12} + C_{13} + C_{14})(\Delta V_2)$, where $\Delta V_2 = \Delta V_3 = \Delta V_4$ and $\Delta V_1 = 0$

b. $Q_2 = (C_{21})(\Delta V_1)$, where $\Delta V_2 = \Delta V_3 = \Delta V_4 = 0$

c. $Q_3 = (C_{31})(\Delta V_1)$, where $\Delta V_2 = \Delta V_3 = \Delta V_4 = 0$ (11)

d. $Q_4 = (C_{41})(\Delta V_1)$, where $\Delta V_2 = \Delta V_3 = \Delta V_4 = 0$

Equation set 11 can be solved for the respective capacitances and providing the capacitance between the split-tip electrodes (C_{21}), again noting $C_{12} = C_{21}$.

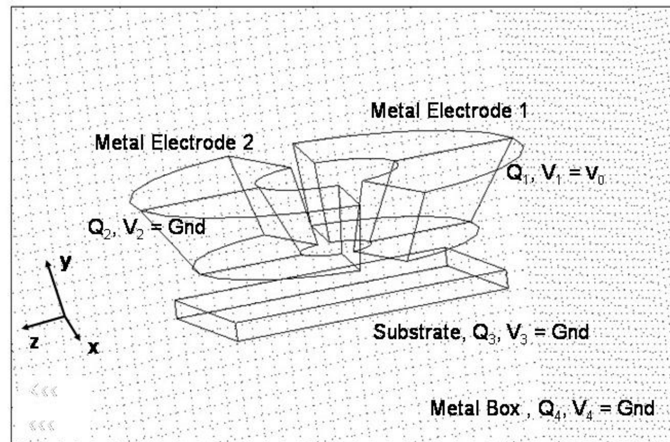

Figure 5. 3: Split-tip probe is located 10nm above the substrate surface. Aluminum and silica substrates were scanned varying the vertical distance in y.

5.2.3 Dopant Density Scans

In this case, we map the dopant density profiles of various n-type doping materials by varying their conductivity. The capacitances are calculated for each material property defined in the model. Since the number of conductors is the same as in the approach scan capacitance model, Equation 10 also applies for the dopant density case. However the boundary conditions are varied, shown in Figure 5.4.

The potential on electrode 1 is set to $+V_0/2$ and the potential on electrode 2 is set to $-V_0/2$. The substrate and metal box have the potential set to ground. Given the boundary conditions have changed, the following set of linear equations are obtained:

a. $Q_1 = C_{12}\Delta V_2 + C_{13}\Delta V_3 + C_{14}\Delta V_4$, where $\Delta V_1 = 0$

b. $Q_2 = C_{21}\Delta V_1 + C_{23}\Delta V_3 + C_{24}\Delta V_4$, where $\Delta V_2 = 0$

c. $Q_3 = C_{31}\Delta V_1 + C_{32}\Delta V_2 + C_{34}\Delta V_4$, where $\Delta V_3 = 0$ (12)

d. $Q_4 = C_{41}\Delta V_1 + C_{42}\Delta V_2 + C_{43}\Delta V_3$, where $\Delta V_4 = 0$

Equation set 12 can be solved for the respective capacitances providing the capacitance between the split-tip electrodes (C_{21}), again noting $C_{12} = C_{21}$.

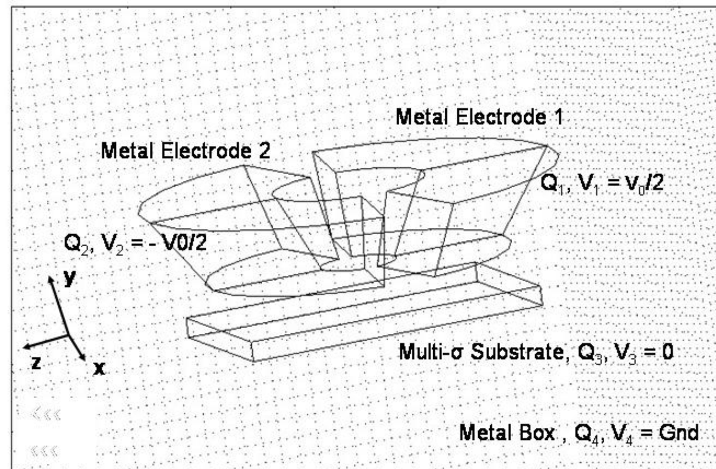

Figure 5. 4: Boundary conditions slightly modified for dopant density measurements. Substrate has conductivity varied and capacitance measurements made.

5.3 Model Results and Discussion

Equation sets 9, 11, and 12 are solved for the capacitance coefficients, and the capacitance between the electrodes ($C_{12} = C_{21}$) is plotted versus distance. Figure 5.5 shows the capacitance between the electrodes from the lateral scans plotted versus distance (+/- x). In this data set, the split is parallel to the nanorod and substrate as described earlier. As the

split-tip probe approaches 0 nm (location of rod and substrate), the capacitance is reduced.

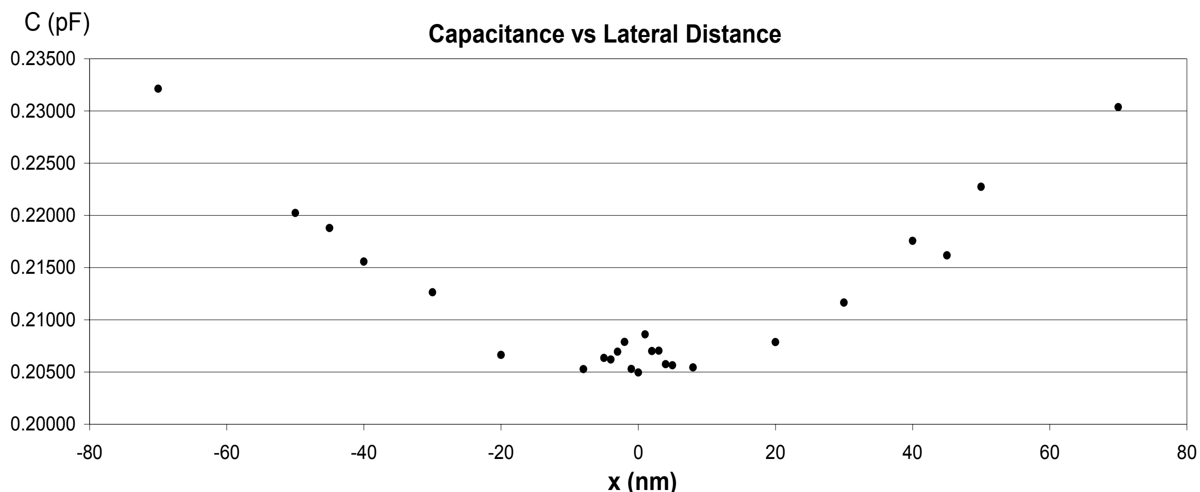

Figure 5. 5: This is a plot of the lateral capacitance between the split-tip probe electrodes with the split parallel to the nanorod and substrate.

Just as the distance reaches 0, there is a slight increase in the capacitance. This is due to the change in distribution of surface charge that occurs. The negative surface charge on the rod and substrate both increase while the surface charge on the uncharged electrode (electrode 2) is decreased. As the conductors (rod and substrate) approach the probe, the surface charges are spread over both orienting themselves with the positive charges located on electrode 1. The displacement of the rod and substrate in the +/- x direction (rastar process) creates

asymmetry in the model, which is minimized by increasing the size of the shielded box.

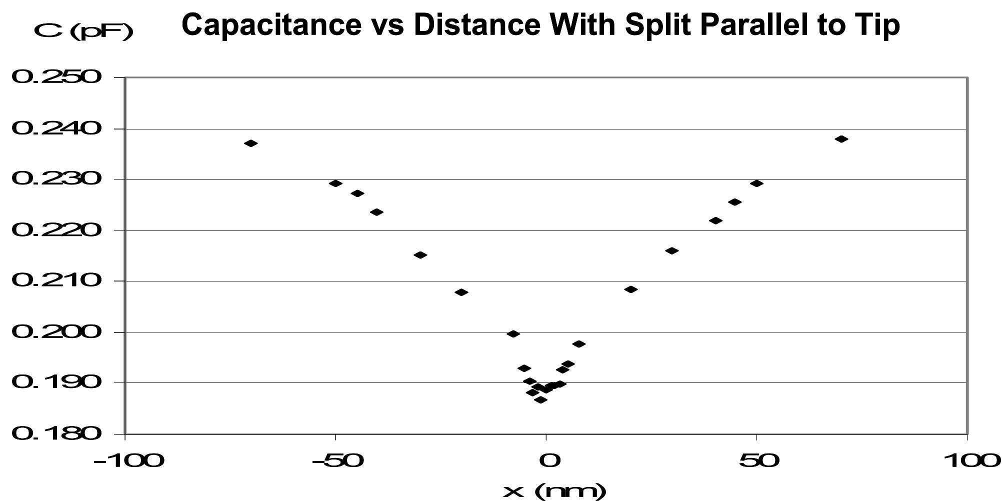

Figure 5. 6: This is a plot of the lateral capacitance between the split-tip probe electrodes with the split perpendicular to the nanorod and substrate.

Figure 5.6 shows the capacitance between the electrodes from the lateral scans plotted versus distance (+/- x). In this data set, the split-tip probes are rotated so that the split is perpendicular to the nanorod and substrate. The profile of the capacitance is similar to profile shown in Figure 5.5, but the capacitance near zero drops abruptly rather than increases.

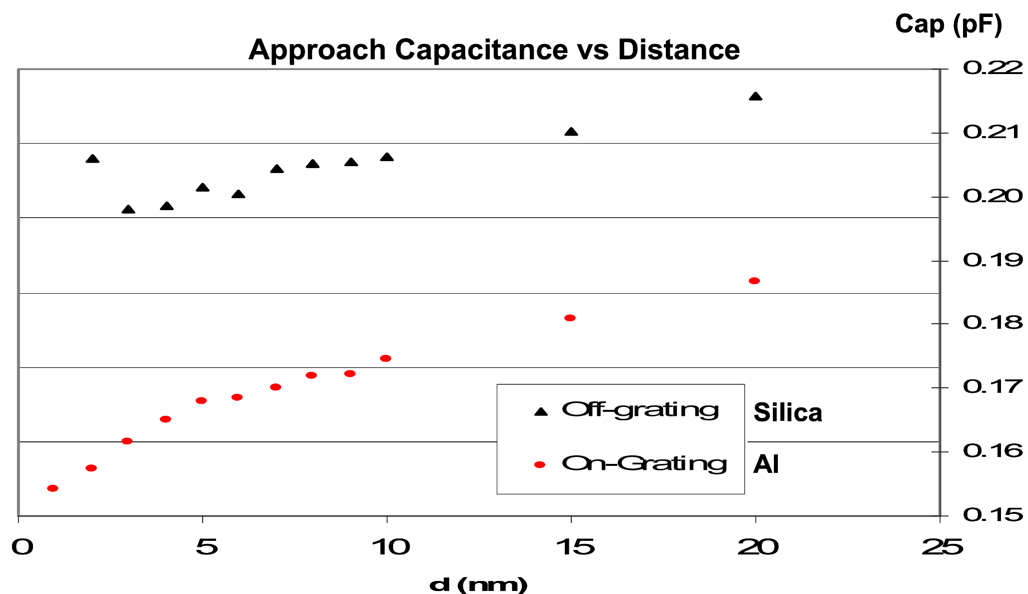

Figure 5. 7: Plot of the capacitance between the electrodes. The horizontal axis shows vertical absolute values labeled d.

Figure 5.7 shows the approach capacitance versus vertical distance for the aluminum and silica samples. The on-grating (aluminum) data represents the capacitance measured as the substrate approaches the split-tip probe. The x axis shows the absolute value for the vertical y distance. The capacitance data from the aluminum substrate (shown in red) decreases as the probe and sample approach one another. This is due to a decrease in negative surface charge on electrode 2 and an increase in negative surface charge on the substrate surface. The decrease in capacitance is slightly more gradual than that of the silicon substrate (shown in black). The overall range of measured capacitance signal is shifted lower than that of the lateral capacitance scans.

To calculate the capacitances for various dopant densities the split-tip (30 nm metal thickness) was held at 3nm above the substrate surface, and the conductivity was changed in the material properties to model the n-type material desired. For each dopant density measured, the capacitance values are show in Figure 5.8. Qualitatively there is a measurable change in capacitance as doping densities are varied. This is promising in the development of a more advanced dopant density mapping scheme.

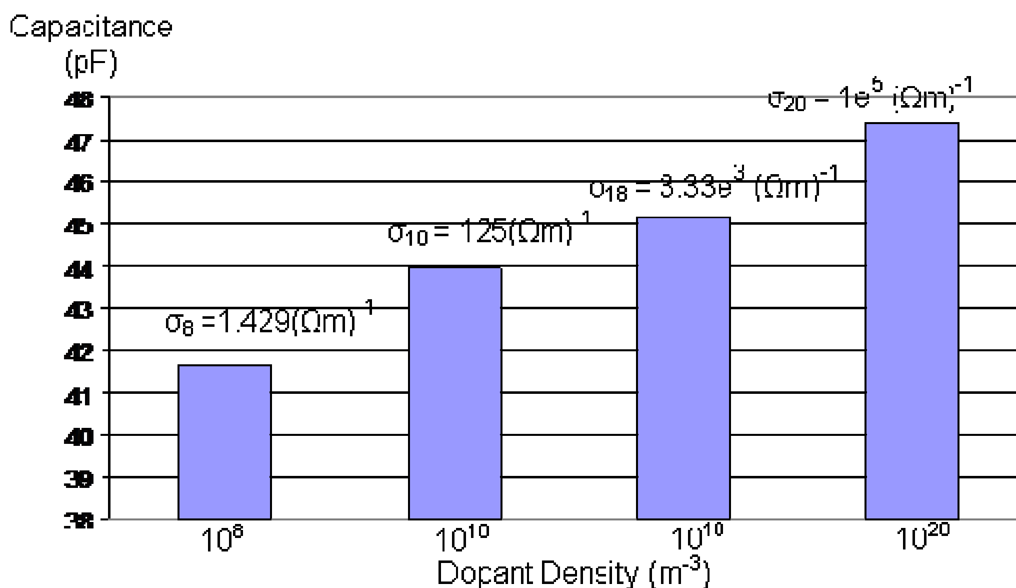

Figure 5. 8: Graph shows the capacitances calculated for n-type materials with different conductivities.

5.4 Data Analysis

The finite element model that has been developed measures charge and capacitance for different tip-sample studies. The model of the split-tip probe and a sample allows for changes to the material property settings and the choice of conducting surfaces with

corresponding boundary conditions. Equation 6, with ΔV_j defined as $V_i - V_j$, provides a linear relation between the electric fields, potentials, and source charges which allows the use of super position to develop a set of equations that define the split-tip system. Since the potentials are defined on all conductors in the system, Equation 6, with proper boundary conditions, can be used to express the charge for each conductor and extract individual capacitance values. The approach capacitance scans establish a basic signal range to be investigated more with the SSCM experimental setup. In the lateral and approach scans, the capacitance profiles are consistent with the behavior of surface charge measured on the conducting surfaces. In all three case studies, measurable capacitance signals were obtained that provide insights into the SSCM experimental approach.

5.5 *Bibliography*

1. C.L. Jahncke and H.D. Hallen, J. Appl. Phys. Lett. **93**, 1274 (2003).

2. E. Betzig and J. Trautman, Science **257**, 189 (1992).

3. A. La Rosa, B. Yakobson, and H. Hallen, Appl. Phys. Lett. **70,** 1656 (1997).

4. D. Cahen and A. Kahn, Adv. Mater. **15**, 271 (2003).

5. X. Wang, Z. Fan, and T. Tang, J. Opt. Soc. Am. A **22**, 2730 (2005).

6. B. Clark III, G. Gurguis, H.D. Hallen, J. Vac. Sci. Technol. B **25**, 54 (2007).

7. S. Bozhevolnyi, J. Opt. Soc. Am. B **14**, 2254 (1997).

8. B. Hecht, H. Bielefeldt, Y. Inouye, and D. Pohl, J. Appl. Phys. Lett. 81, 2492 (1997).

9. J. Trautman, E. Betzig, J. Weiner, D. DiGiovanni, T. Harris, F. Hellman, and E. Gyorgy, J. Appl. Phys. Lett. **71**, 4659 (1992).

10. S. Lanyi and M. Hruskovic, J. Phys. D: Appl. Phys. **36**, 598 (2003).

11. P. Pomorski, C. Roland, H. Guo, and J. Wang, Phys. Rev. Lett. B **67,** 161404-1 (2003).

12. H. Ruda and A. Shik, Phys. Rev. Lett. B **67**, 235309 (2003).

13. M. Heald and J. Marion, *Classical Electromagnetic Radiation*, (Thompson Learning, USA, 1995), 3rd ed.

Chapter 6

6. Split-Tip Scanning Capacitance Microscopy (SSCM)

6.1 Introductory Split-Tip Scanning Capacitance

Split-tip scanning capacitance microscopy (SSCM) offers interesting advantages over other scanning probe methods. SSCM differs from the related, single tip Atomic Force Microscopy (AFM) based version by having both electrodes located on the tip. This reduces the dependence of the measurement on the sample characteristics and thus simplifies analysis. SSCM allows the imaging of simultaneous topographic, optical, and electronic structures. This feature allows non-conducting, as well as conducting surfaces to be imaged

without loss of optical resolution [1-4]. The split-tip is a dual electrode probe that allows measurements in a non-contact manner.

Split-tip capacitance measurements as a function of tip-sample separation provide a critical and discerning test of the models and instrument capabilities. Approach capacitance measurements show the ability to distinguish between different sample surfaces by measuring the capacitance between the probe electrodes and how it varies with respect to the distance from the sample surface. We present approach capacitance measurements made on a sample comprised of aluminum structures deposited on a silica substrate [5-8].

6.2 SSCM Split-tip Holder

The SSCM was developed from a conventional NSOM setup in an effort to create an additional scanning probe tool that would provide electrical characteristics of nanostructures and have other correlation scan modes as well. Figure 6.1 shows the initial NSOM setup constructed prior to split-tip probe modifications. In developing the SSCM setup, a split-tip probe and holder was designed to replace the glass holders used in our NSOM setups. The conventional holders did not have a self-contained probe mounting system or electrical connections.

In order to secure a probe to the tuning fork, an external mounting tool was needed. While single contact measurements were possible (with silver paint and 2mm diameter gold wire), conventional holders provided no means of making electrical contacts to multiple

electrodes. Ultimately this need for a secured multi-contact holder gave rise to the fabrication of the V-groove clamp used in SSCM. Additionally a capacitance bridge circuit

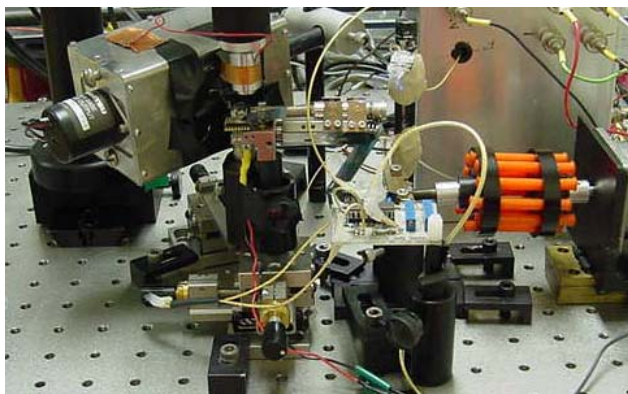

Figure 6. 1: Image of Standard NSOM setup with PMT (top left) used for optical data collection. The probe and tuning fork are mounted to the glass tip holder, with the sample mounted to the piezo electric tube for fine adjustment (top center). Course adjustment is achieved with a stepper motor (right middle).

was designed and integrated into the system to read the signal from the split-tip probe.

The split-tip holder (shown in Figure 6.2) allows independent electrical contact to each side of the split-tip and a means to verify contact and lack of shorting between the two electrode sides. The two metal leads on each side of the holder are used to verify contacts. This is an important process given the V-groove clamp that houses the metal leads and split-tip probe will be adjusted to secure the probe to the tuning fork. The V-groove clamp is made from Teflon and held to a glass plate by three , a spring, and two Sapphire hemispheres attached to the bottom of the glass plate. The V-groove allows the split-tip probe to rest securely keeping the lower electrode of the probe positioned on the metal contacts. It is important screws that the electrodes on the fiber not slide on the metal leads or the evaporated metal on the fiber will wipe off, destroying the electrical connection.

There is an additional Teflon cover secured by screws providing contacts to the top split-tip electrode. This entire two-part Teflon fixture can be translated and rotated with three screws to bring the fiber probe up against the tuning fork [9-13].

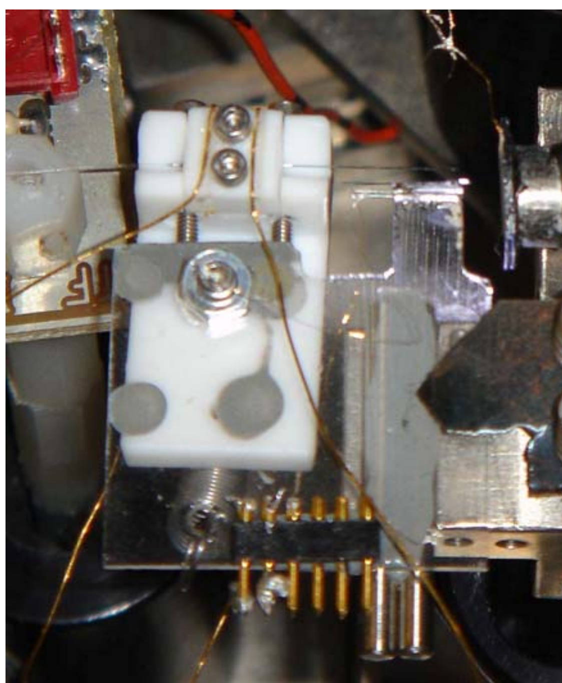

Figure 6. 2: Split-tip can be adjusted to make attachment to the tuning fork tip holder used in SSCM. Holder has adjustable V-groove clamp to secure the split-tip.

Both the fixture and tuning fork are mounted to a glass plate (Figure 6.2) that fits onto the SSCM. The probe tip is glued onto the side of a quartz tuning fork (a few mm in length, with 32768 Hz free resonance). Once the probe is against the tuning fork, glue is applied to the joint and the adjustments left fixed. A drop of epoxy applied to the base of the tuning fork improves stability. We have found that the clamping of the fiber as shown in Figure 6.2

does not impair the lateral force microscopy of the SSCM, nor has there been any significant differences observed in the resonance behavior of the split-tips compared to uncoated or uniformly-coated NSOM probes.

6.3 Capacitance Sensor

The capacitance bridge circuit used in the SSCM experimental setup is critical in reading the small capacitance value from the split-tip probe. The SSCM uses a Universal Capacitive Readout IC (MS3110) ultra-low noise CMOS integrated circuit. This circuit is designed for use in MEMS sensors and other related devices to read variable capacitance. The capacitance bridge circuit is capable of sensing capacitance changes down to 4.0aF/rtHz, well within the range of our measurable signal (pF range). This circuit also provides trim for gain and output offset. The capacitance bridge circuit was mounted on a lab-made PC board and calibrated with a lab-written Labview program.

6.4 Sample Grating

With the split-tip probe, split-tip probe holder, and capacitance bridge circuit fully developed, the rest of the chapter will focus on acquisition of experimental data. Split-tip capacitance measurements with respect to tip-sample distance provide a much more critical test of the physical models and instrument capabilities than imaging, so we focus on those. More specifically, approach capacitance measurements show the ability to distinguish between different sample surfaces by measuring the capacitance between the probe electrodes and how it varies with respect to the distance from the sample surface. There were

approach capacitance measurements made on a sample comprised of aluminum structures deposited on a silica substrate. The aluminum structure has a pitch and length of 10μm respectively. The pitch is defined as the spacing in y that is measured from the front edge of one grating to the back edge of another. The length is defined as the spacing in x that is measured from the back edge of one grating to the front edge of another. It also has a depth of 180nm, which is the spacing in z measured from the top of the aluminum grating to the floor of the substrate (silica). Capacitance measurements were taken while positioned over the aluminum and silica substrate structures.

6.5 Measurement Sequence

To take approach capacitance measurements with the SSCM system, we start by bringing the system into stable feedback (discussed in Chapter 2) with the proper choice of operational resonance frequency. The SSCM setup uses a tuning fork oscillator to detect the split-tip oscillation amplitude and control the separation of the split-tip and sample. Upon achieving proper feedback, sections of the sample are topographically scanned to identify structures of interest (in this case either aluminum grating structures or silica substrate regions). Once sections of interest are identified, the split-tip probe is moved and 'held' in lateral position allowing for only vertical movement regulated by the shear-force split-tip/sample response. Variable z monitor is manually adjusted while the capacitance, topography, and z values are being collected. Variable z monitor controls the approach direction, and special caution is taken to increase/decrease variable z monitor in a semi-

constant rate for clarity in data interpretation. The rate at which variable z monitor is changed has no affect on the feedback response, given the response is faster than the variable z monitor rate of change.

Capacitance values are continuously recorded as the vertical position (defined as z for SSCM experimental setup) is varied. This process is repeated for other regions of interest.

6.6 SSCM Experimental Results

In this study, two regions of interest were studied on the sample: the aluminum grating structure and the silica substrate structure. When the approach scan process is initiated, capacitance (pF) and z (nm) values are recorded. To verify the location of the split-tip probe (either over aluminum grating or silica substrate), the z range and surface features are investigated and compared to the grating dimensions presented earlier.

Figure 6.3 shows experimental capacitance values plotted versus topography for aluminum. Also shown is the z range versus topography. There were 2000 data points read

in over a 750nm z range.

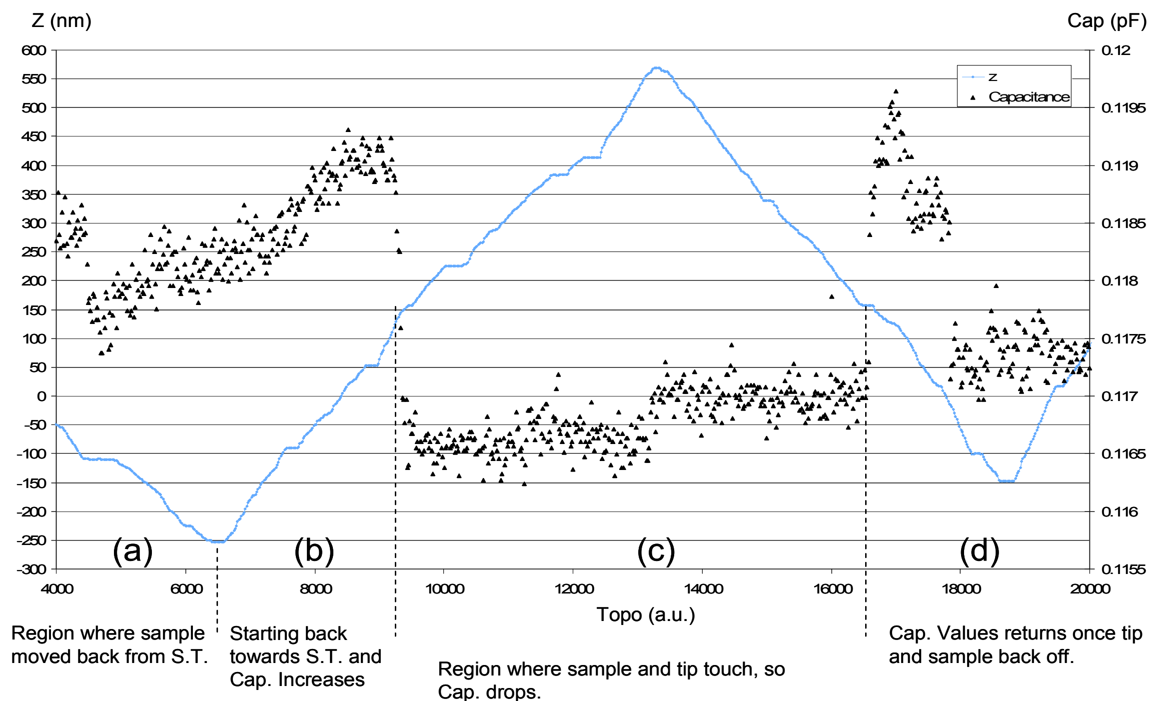

Figure 6. 3: This is a plot of the experimental data taken from the aluminum grating structure. There were 2000 capacitance points read in over a 750nm z-range.

To gain a better knowledge of the entire data range, the plot is divided into four sections (a,b,c,d) for analysis. The data plotted in blue is the z values measured in nanometers, and the capacitance values are shown in black. Z describes the motion of the sample (z piezo voltage) as the scan progresses in topography. In region (a), from the decreasing z values, we note that the sample is moving back from the split-tip. As discussed in Chapter 3, it is important to note that the fine adjustment to the scan process is done to the sample, and not the probe. Region (b) is where the sample starts back toward the split-tip probe, and there is an increase in capacitance. Around the z value of 173nm (the start of region c), there is an

extreme reduction in the capacitance values. Region (c) shows the capacitance values decreased due to the tip and sample touching. This is defined as a ‘soft crash’ into the sample as opposed to a ‘hard crash’ of the probe as discussed in other scanning probe techniques (Chapter 3). Soft crashes (in regions much larger than the tip size) do little or no damage to the split-tip electrodes or sample. The sample simply deflects due to the relative tip-sample motion. This is remedied by backing away from the split-tip probe, and the 1/r behavior seen prior to the soft crash is restored, as shown in region (d). There is an overall measured signal change of 3.45f F (10^{-15} F), which is well above the 4aF (10^{-18} F) sensitivity limit of the capacitance bridge circuit.

To gain more insights into the data obtained, it is necessary to plot capacitance and z versus sample point. This shows how the capacitance varies with split-tip probe/sample proximity for each data point taken. Regions (a) and (b) from Figure 6.3 are of particular interest because they show capacitance values and their response to the soft crash of the split-tip probe. Figure 6.4 shows the capacitance versus z plotted for parts of regions (a) and (b) of Figure 6.3. Again there is a drastic decrease in the capacitance values around a z value of 173 nm, which is the soft crash point. Therefore for the entire data set range of z values measured, we can deduce that the aluminum grating structure is located at

approximately z = 173nm.

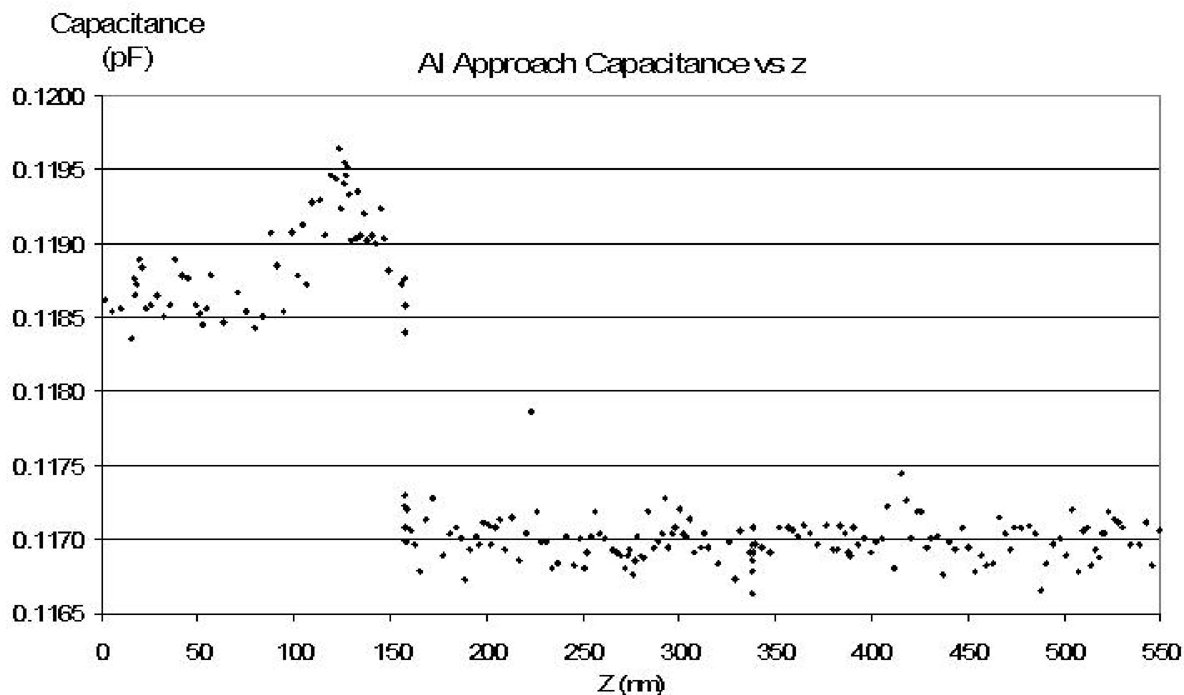

Figure 6. 4: Plot of approach capacitance versus z from the aluminum grating structure. The 0-550nm range spans over regions (a) and (b) from Figure 6.3.

So to define "zero" as the lowest point on the aluminum grating structure (i.e. the surface of interest), the values would have to be offset by approximately 173nm. Also noting that there is some drift in the experimental data (due to drift from the capacitance bridge circuit), we can correct for the tilt and shift the data to accurately reflect the location of the sample surface. Figure 6.5 shows the experimental data set from Figure 6.3, but with the sample surface correctly shifted to z = 173nm and the drift from the capacitance bridge circuit removed. From Figure 6.5, it is straightforward to see that at sample point 450 (approximately 225nm), the capacitance values decline sharply corresponding with the soft

crash into the sample surface, and also return once the split-tip gains separation from the sample surface (at sample point 800), which is also located at 225nm.

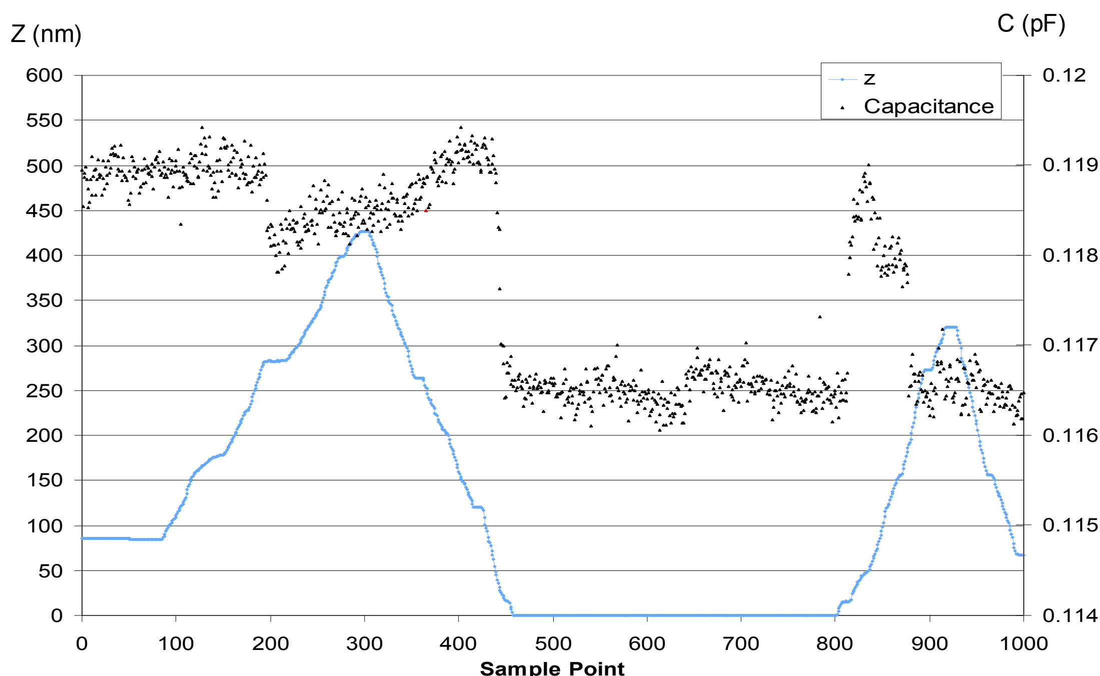

Figure 6. 5: This is a plot of the experimental data taken from the aluminum grating structure (shown in Figure 6.3) with the sample surface correctly shifted to z = 173nm and the drift from the capacitance bridge circuit removed.

The fact that the soft crash point and capacitance restoration point have the same z value indicates that drift from the capacitance bridge circuit had minimal to no effect on the experimental data values. To compare various capacitance data sets taken near the surface, the capacitance is plotted as a function of the z values. Figure 6.6 compares capacitance profiles for two different data sets taken near the sample surface. Both sets show that as the split-tip gains separation from the surface, the capacitance values initially increase. After

approximately 50nm of separation distance, the capacitance values start to decrease as z increases.

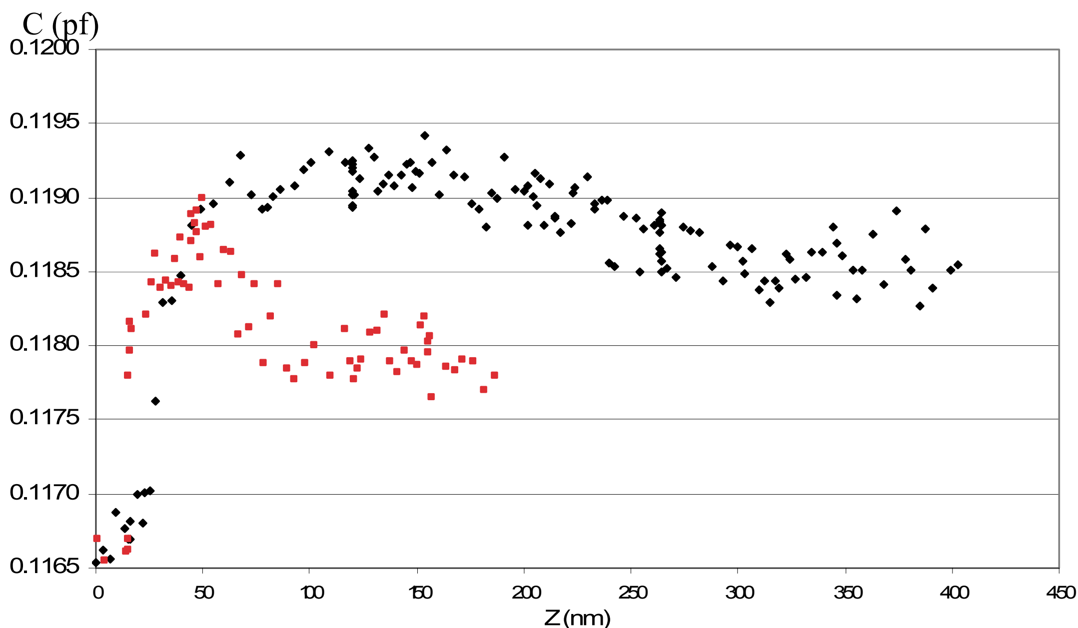

Figure 6. 6: Plot shows various aluminum capacitance profiles taken from Figure 6.5. Plot compares capacitance profiles for two different data sets taken near the sample surface. The vertical axis shows Capacitance (pF) and z (nm), shown on the horizontal axis, give the distance near the sample surface.

Figure 6.7 shows experimental capacitance and z values plotted versus topography for silica. Before the sample and split-tip probe touch, the overall range of capacitance values for silica is shifted higher than those for the aluminum. At z = 175nm, there is a reduction in the capacitance values. The fact that the soft crash point is not the same for the aluminum and silica is to be expected. This is due in part to the fact the aluminum grating is taller than the silica substrate and mostly to the fact that the sample is tilted (due lesser to some thermal drift in z between the measurements). In any case, defining "zero" as the lowest point on the

sample of interest is a matter of correcting z by the offset value z_0, which is 175 nm for the silica data set.

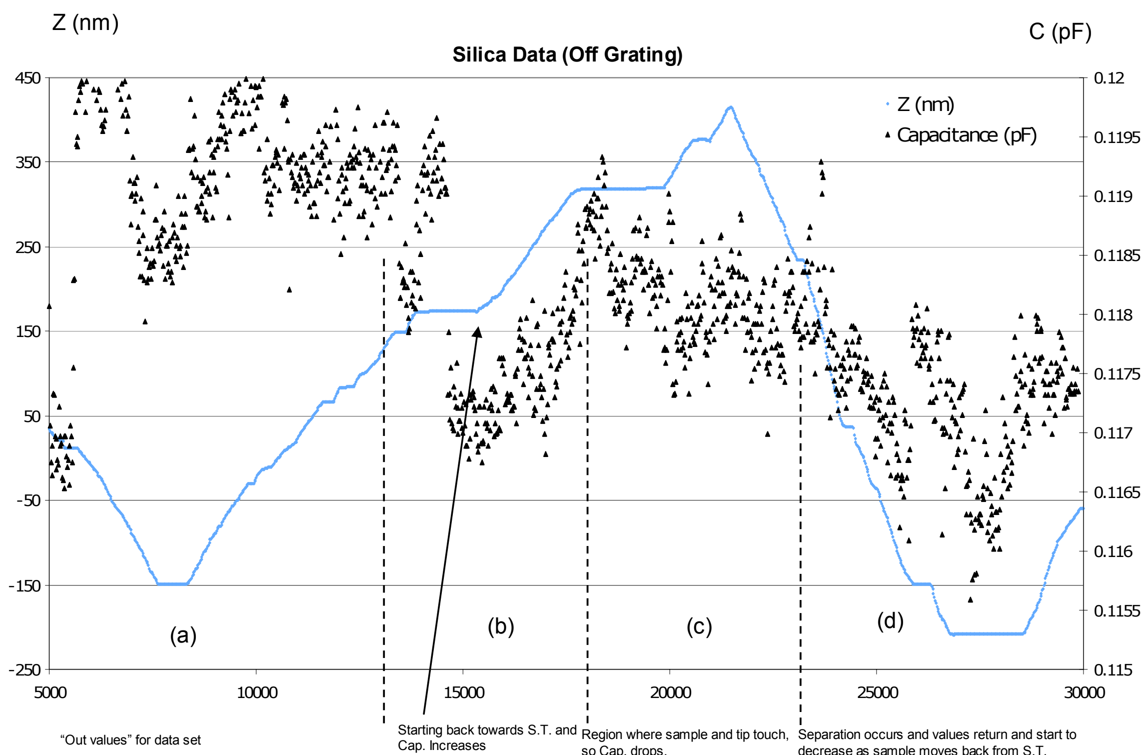

Figure 6. 7: This is a plot of the experimental data taken from the silica grating structure. There were 2000 capacitance points read in over a 750nm z range.

Figure 6.8 shows a plot of the silica approach capacitance versus z values (taken from region (b) of Figure 6.7). At z =175nm, there is an immediate reduction in the capacitance signal from the soft crash, and after split-tip/sample separation is achieved, the capacitance values are restored. Figure 6.9 compares silica capacitance profiles for two different data sets taken near the sample surface. Figure 6.9 shows and compares various silica capacitance data sets

taken near the surface. As with the aluminum data, the capacitance is plotted as a function of the z values to more accurately compare the capacitance profiles near the sample surface.

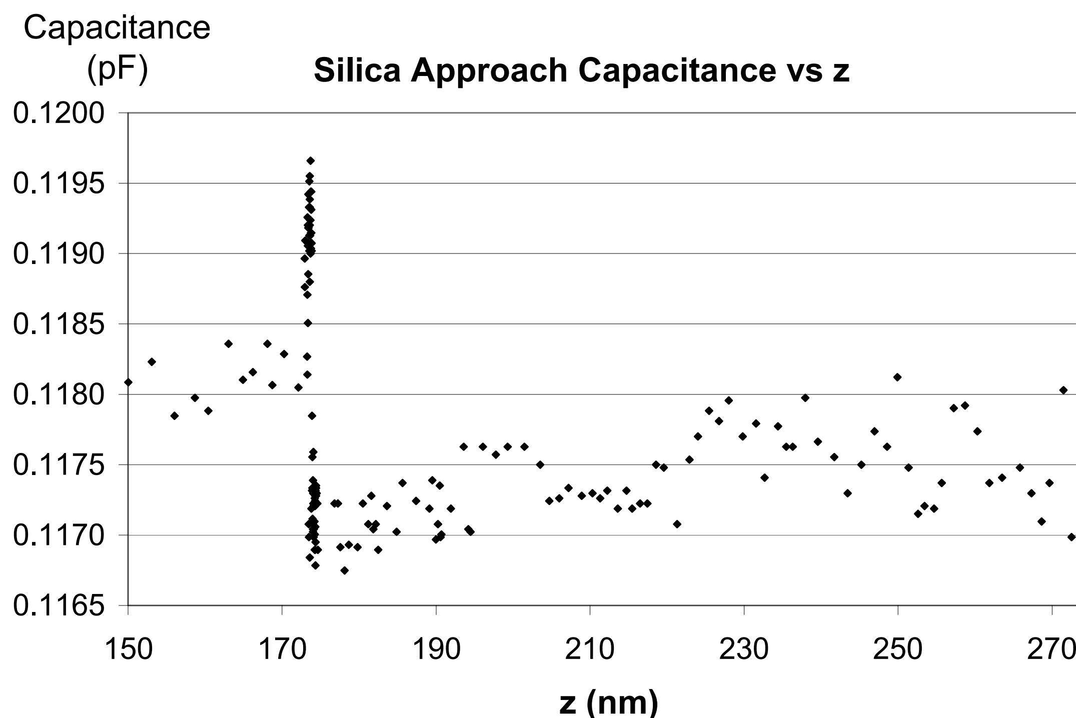

Figure 6. 8: Plot of the silica approach capacitance versus z values taken from region (b) of Figure 6.7.

Both sets show that as the split-tip gains separation from the sample surface, the capacitance values are initially larger, decreasing as the z values increase. This behavior for silica is opposite of that seen for aluminum. Figure 6.10(a) shows that for the first 25 nm of split-tip/sample separation, the capacitance values for the aluminum initially start low and increase and the capacitance values for the silica initially start high and decrease. Comparing Figure 6.10(a) to Figure 6.10(b), we see that both the aluminum and silica experimental data follow the capacitance profiles shown in the Femlab model.

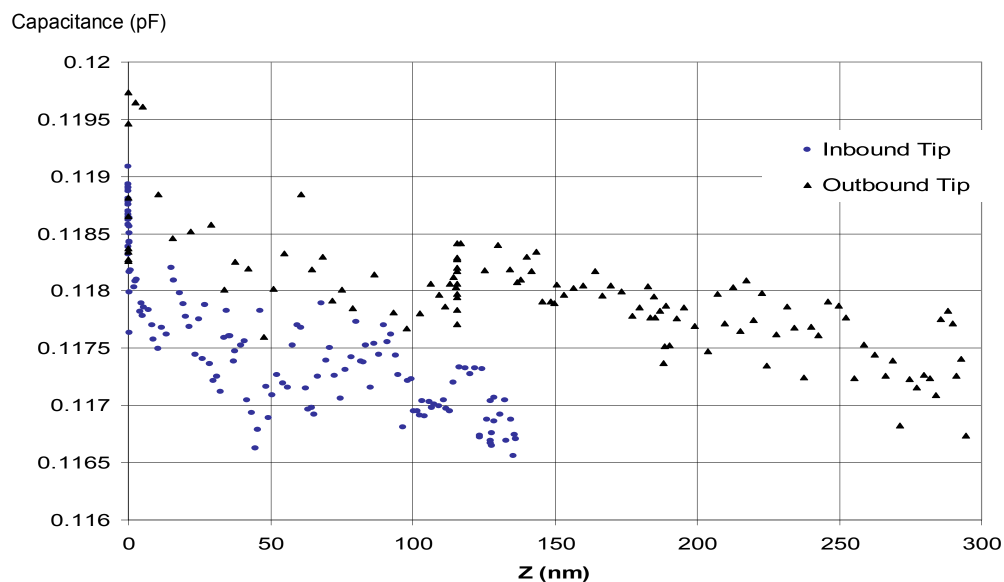

Figure 6. 9: Plot shows various silica capacitance data sets taken near the surface. The capacitance is plotted as a function of the z values to more accurately compare the capacitance profiles near the sample surface.

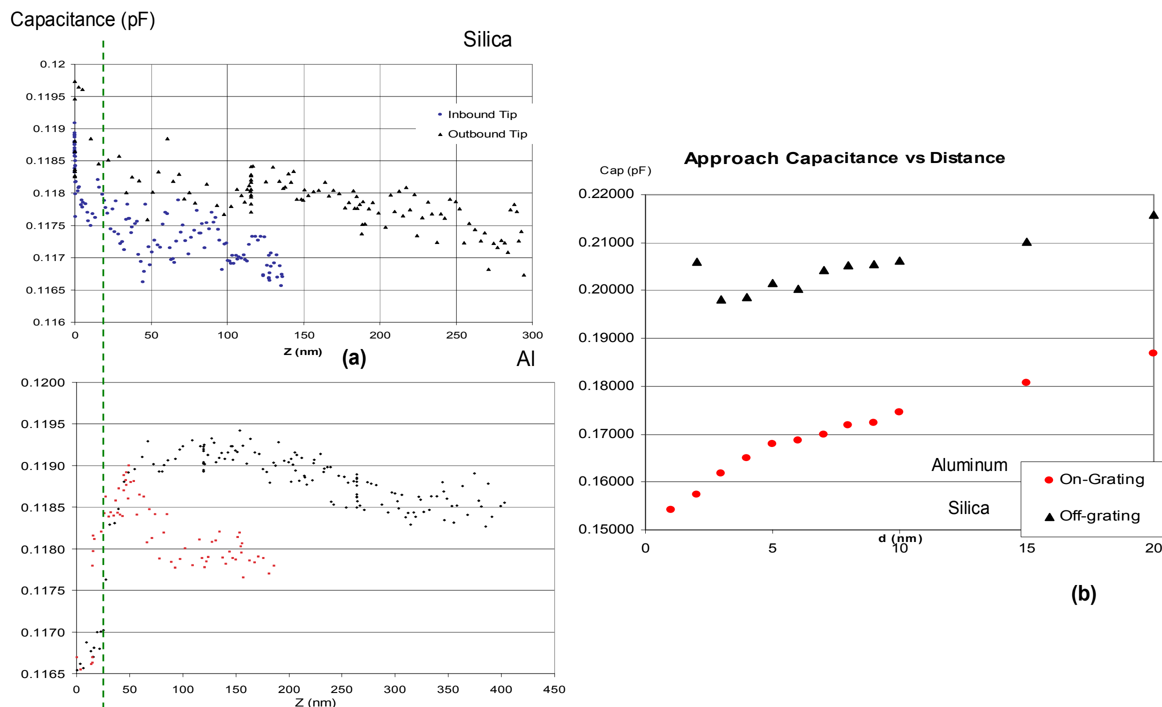

Figure 6. 10: Plots compare various experimental capacitance profiles from aluminum and silica sample scans to the Femlab model values. The green line indicates the range of data comparable to the Femlab model, which is the first 25nm of capacitance values.

The Femlab model for the aluminum shows low capacitance values initially near the sample surface with an increase over the next 25 nm, which is consistent with the aluminum SSCM experimental data. The Femlab model for the silica shows high capacitance values initially near the sample surface with a decrease over the next 25 nm, which is also consistent with the silica SSCM experimental data. For values near the sample surface, the Femlab model appropriately predicts the capacitance profiles for both samples. Figure 6.11 shows the Femlab aluminum model data plotted with the inbound/outbound aluminum experimental data.

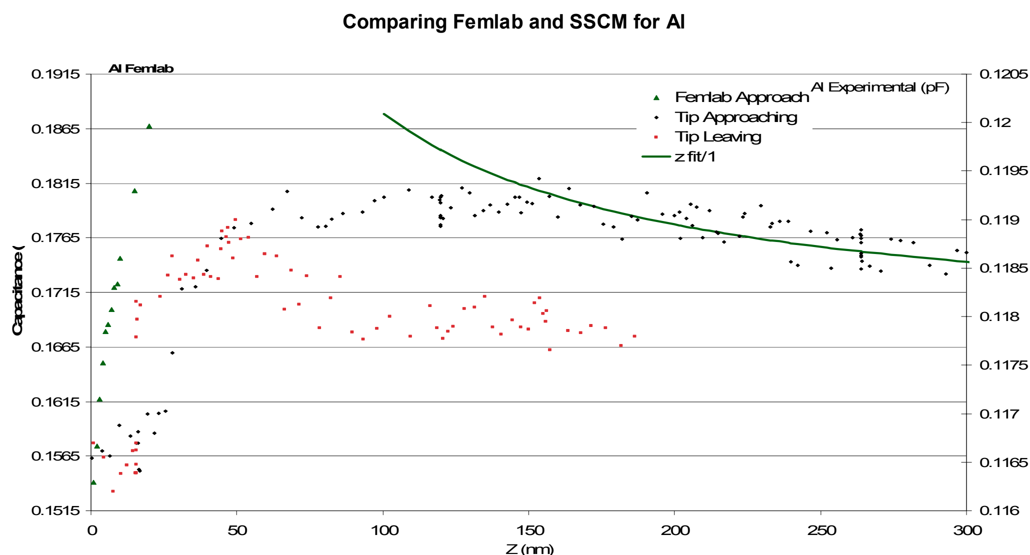

Figure 6. 11: Femlab aluminum model data plotted with the inbound/outbound aluminum experimental data. 1/z curve (solid line) is fit to one set of the aluminum experimental data, which appropriately describes the behavior of the aluminum experimental data well away from the sample surface.

Looking at the aluminum model and experimental data, we note that close the the surface, the Femlab model appropriately predicts the capacitance profile, and once the separation distance is greater than 150nm, the capacitance profile for the aluminum SSCM data decreases following a 1/z functional form (shown in Figure 6.11). Figure 6.11 shows a 1/z curve (solid line) fit to one set of the aluminum experimental data, which appropriately describes the behavior of the aluminum experimental data well away from the sample surface.

6.7 SSCM Data Analysis

From Figure 6.4, we gain clear insights into the capacitance behavior of the aluminum grating structures by plotting the approach capacitance versus z data. The data

shows a decrease in capacitance values due to the split-tip probe/sample interaction called a soft crash. Once separation is obtained between the split-tip probe and sample the capacitance values are restored (collectively shown in Figure 6.3). Similar profiles are observed for the silica substrate as well. In comparing the silica and aluminum approach capacitance values just before the soft crash, we see the silica values start slightly lower and finish slightly higher than those of the aluminum grating. The aluminum capacitances (prior to soft crash) range from 0.1184pF to 0.1196pF, seen in Figure 6.4 and the silica approach capacitances range from 0.1179pF to 0.1197pF, seen in Figure 6.8. In both cases, there is a clear z value that signifies soft crash effects resulting in a decrease in signal. This value defines the offset value for "zeroing" the sample of interest location, when necessary. There is an overall measurable signal of 3.45fF for the aluminum substrate, and 4.50fF for the silica substrate.

6.8 Bibliography

1. J. Trautman, E. Betzig, J. Weiner, D. DiGiovanni, T. Harris, F. Hellman, and E. Gyorgy, J. Appl. Phys. Lett. **71**, 4659 (1992).

2. X. Wang, Z. Fan, and T. Tang, J. Opt. Soc. Am. A **22**, 2730 (2005).

3. E. Betzig and R. Chichester, Science **262**, 1422 (1993).

4. S. Bozhevolnyi, J. Opt. Soc. Am. B **14**, 2254 (1997).

5. P. Pomorski, C. Roland, H. Guo, and J. Wang, Phys. Rev. Lett. B **67,** 161404-1 (2003).
6. H. Ruda and A. Shik, Phys. Rev. Lett. B **67**, 235309 (2003).

7. P. Pomorski, L. Pastewka, C. Roland, H. Guo, and J. Wang, Phys. Rev. Lett. B **69**, 115418 (2004).

8. S. Lanyi and M. Hruskovic, J. Phys. D: Appl. Phys. **36**, 598 (2003).

9. K. Karrai and R. Grober, Proc. SPIE **2535**, 69 (1995).

10. K. Karrai and R. Grober, Appl. Phys. Lett. **66**, 1842 (1995).

11. D. Sarid, *Scanning Force Microscopy* (Oxford University Press, New York, 1991), 1st ed.
12. R. Toledo-Crow, P. Yant, Y. Chen, and M. Vaez-Iravani, Appl. Phys. Lett. **60**, 2957 (1992).

13. M. Heald and J. Marion, *Classical Electromagnetic Radiation*, (Thompson Learning, USA, 1995), 3rd ed.

Chapter 7

7. Dissertation Conclusions

The shear force feedback methods discussed in Chapter 2 provide ample feedback response to successfully operate the SSCM experimental setup. The nonlinear model accurately describes both the system dynamics and the resonance curve behavior as the probe approaches the sample. During this approach the probe taps on surface adsorbed layers prior to tapping on the surface itself. This implies that the lateral force feedback is a good indicator of tip-sample distance when small oscillation amplitudes are used, and that a tapping mechanism describes the nonlinearity of the tip-sample interaction.

The study and characterization of irregular surfaces was insightful in establishing a process for statistical analysis that yielded information about the mesoscale order of pigment distributions and also provided needed insight into the optical resolution of the scanning probe system. The NSOM approach for sample identification and characterization was

effective in allowing us to resolve features in the mesoscale regime, which distinguish high and low quality paints and has potential applications to other studies.

The finite element model that has been developed successfully measures charge and capacitance for different tip-sample studies. The model of the split-tip probe and sample allows for changes to the material property settings and the choice of conducting surfaces with corresponding boundary conditions. Fundamental physics relations provide a linear relation between the electric fields, potentials, and source charges allowing the use of super position to develop a set of equations that define the split-tip system. In the lateral and approach scans, the capacitance profiles are consistent with the behavior of surface charge measured on the conducting surfaces. In all three case studies, measurable capacitance signals were obtained that provide insights into the SSCM experimental setup.

The addition of this newly invented scanning probe technique into the world of nanoscale characterization will provide additional tools for nanoscale studies. The split-tip probe itself has multiple applications including deposition of in-plane orientated nano-patterned molecules and characterization, in addition to SSCM studies. The probe mounts into and expands the versatility of conventional scanning probe techniques such as NSOM and SSCM. The fabrication is significantly more difficult for SSCM probes, but the result provides a wealth of applications within the scanning-probe scheme, justifying the construction. The fabricated split-tip probes perform well in topographic and optical microscopy in addition to the unique functions enabled by the split-tip. This in turn, also provides a means for electro-optical studies.

This dissertation presents the first ever approach capacitance scans taken using the novel split-tip nanoprobe and capacitance bridge circuit integrated into a conventional NSOM system. The idea of making electric measurements to the surface of a sample is made far more convenient with the SSCM method, given the minimum preparation needed to the samples of interest, the versatility in sample selection for study, and the potential to acquire data through multiple, simultaneous scanning modes.

In conclusion, the SSCM experimental setup proved adequate in the testing and measuring of the aluminum grating structure and silica substrate. The fabrication and design of the V-groove holder to secure the optical nanoprobe used in the SSCM setup was successful in allowing independent contacts to be made to split-tip electrodes. From analyzing both sets of data, the results are promising in expanding the range of samples studied. Approach capacitance measurements show the ability to distinguish between different sample surfaces by measuring the capacitance between the probe electrodes and how it varies with respect to the distance from the sample surface. The measurable signal change seen in the capacitance measurements serve as an appropriate discriminating characteristic for identifying samples of interest.